# Plastic Deformation and Recrystallization of Garnet: A Mechanism to Facilitate Diffusion Creep

## C. D. STOREY[1]* AND D. J. PRIOR[2]†

[1]DEPARTMENT OF GEOLOGY, UNIVERSITY OF LEICESTER, UNIVERSITY ROAD, LEICESTER LE1 7RH, UK

[2]DEPARTMENT OF EARTH AND OCEAN SCIENCES, UNIVERSITY OF LIVERPOOL, LIVERPOOL L69 3GP, UK

*Elongate and deformed garnets from Glenelg, NW Scotland, occur within a thin shear zone transecting an eclogite body that has undergone partial retrogression to amphibolite facies at circa 700°C. Optical microscopy, back-scattered electron imaging, electron probe microanalysis and electron back-scatter diffraction reveal garnet substructures that are developed as a function of strain. Subgrains with low-angle misorientation boundaries occur at low strain and garnet orientations are dispersed, around rational crystallographic axes, across these boundaries. Towards high-strain areas, boundary misorientations increase and there is a loss of crystallographic control on misorientations, which tend towards random. In high-strain areas, a polygonal garnet microstructure is developed. The garnet orientations are randomly dispersed around the original single-crystal orientation. Some garnet grains are elongate and Ca-rich garnet occurs on the faces of elongate grains oriented normal to the foliation. Commonly, the garnet grains are admixed with matrix minerals, and, where in contact with other phases, garnet is well faceted. We suggest that individual garnet porphyroclasts record an evolution from low-strain conditions, where dislocation creep and recovery accommodated deformation, through increasing strain, where dynamic recrystallization occurred by subgrain rotation, to highest strains, where recrystallized grains were able to deform by diffusion creep assisted grain boundary sliding with associated rotations.*

KEY WORDS: *diffusion creep; EBSD; garnet; plastic deformation; recrystallization*

## INTRODUCTION

Microstructures in deformed rock-forming minerals are crucial in aiding our understanding of the rheology of the bulk Earth. Garnet is a particularly important mineral, in both the crust and the mantle. It is a key constituent of eclogite at the base of thickened continental crust and within subducted crustal slabs, upper mantle peridotites and in the mantle Transition Zone (majoritic garnet) at depths of 400–650 km (Karato & Wu, 1993; Vauchez & Mainprice, 1996) and may control mantle rheology (Karato et al., 1995). Additionally, garnet is a key mineral in many metamorphic rocks.

Garnet chemistry is used directly in many geothermobarometers (Pattison & Tracy, 1991; Spear, 1992) and in radiometric dating (Vance & Onions, 1988, 1990; Vance & Holland, 1993; Christensen et al., 1994; Vance, 1995; DeWolf et al., 1996; Vance et al., 1998; Scherer et al., 2000). Linking such data to the microstructural relationships of garnet porphyroblasts, their inclusions and external fabrics is often crucial to establishing pressure–temperature–time ($P$–$T$–$t$) paths of metamorphic terranes (e.g. Spear & Selverstone, 1983; Daly et al., 1989; Okudaira, 1996; Marshall et al., 1997; Vance & Mahar, 1998; Kohn et al., 2001). Hence, understanding the behaviour of garnet under high-strain conditions is critical to understanding both deformation and metamorphism in the mid to lower crust and in the upper mantle.

Until recently, our understanding of the deformation mechanisms of rock-forming minerals has been largely restricted to anisotropic crystallographic phases that can be studied using optical microscopy. Although the early Laue diffraction studies of flattened garnets in mylonites (Dalziel & Bailey, 1968; Ross, 1973), etching (Carstens, 1969, 1971) and transmission electron microscope (TEM) studies of natural garnet (Smith, 1982; Allen et al., 1987; Ando et al., 1993; Doukhan et al., 1994; Voegele et al., 1998a, 1998b, 1999, 2000) have suggested various mechanisms responsible for elongation, it is only recently, with the advent of scanning electron microscope (SEM)-based

*Present address: Department of Earth Sciences, The Open University, Walton Hall, Milton Keynes MK7 6AA, UK.

†Corresponding author. Telephone: +44 (0)151 794 5193. Fax: +44 (0)151 794 5196. E-mail: davep@liv.ac.uk

techniques such as electron channelling (Lloyd, 1987; Lloyd *et al.*, 1991*a*, 1991*b*) and electron back-scatter diffraction (EBSD: see Venables & Harland, 1973; Dingley, 1984; Prior *et al.*, 1999, 2002) that crystallographic data can be readily obtained from cubic (isotropic) minerals such as garnet. These new technologies have led to a recent resurgence of interest in garnet deformation mechanisms.

Elongate garnets have been observed in a wide range of *P–T* environments from greenschist-facies (Azor *et al.*, 1997) to granulite-facies (Ji & Martignole, 1994) and eclogite-facies (Ji *et al.*, 2003). In granulite-facies garnets, deformation is interpreted to be due to plastic deformation, on the basis of TEM work that showed some subgrain structures (Ji & Martignole, 1994). Kleinschrodt and co-workers (Kleinschrodt & McGrew, 2000; Kleinschrodt & Duyster, 2002) have demonstrated that elongate garnets within granulite-facies quartzites from Sri Lanka have a weak crystallographic preferred orientation (CPO). However, these garnets exhibit little sub-structure and, as such, convincing deformation mechanism information derived from these samples is fairly restricted. Garnets in eclogites (Ji *et al.*, 2003; Mainprice *et al.*, 2004) also have weak CPOs—much weaker than the fabrics predicted by a visco-plastic self-consistent model that uses dislocation systems identified in the same samples using TEM. Mainprice *et al.* (2004) concluded that although garnet deformed by dislocation creep and recovery, the other minerals (omphacite and quartz) accommodated a significant proportion of the deformation. Prior *et al.* (2000) have shown that mantle garnets contain significant sub-structures that are best explained by high-temperature dislocation creep and recovery. Prior *et al.* (2002), during an earlier study on the Glenelg eclogite sample that will be examined further in this paper, suggested that elongate garnet within crustal rocks is also best explained by dislocation creep and recovery. These recent studies have served to convince us that crystal-plastic deformation can account for elongation of garnet under certain conditions, yet the precise deformation mechanisms and conditions are yet to be determined. Terry & Heidelbach (2004) have shown recently that fine-grained garnet can deform by grain boundary sliding with grain boundary migration as an associated mechanism. In their study, garnet grain sizes varied from about 30 μm at low strains to <10 μm at high strains and they showed evidence that garnet growth occurred during deformation. A key question that remains is whether garnet, when deformed to high strains, will recrystallize in a similar way to other rock-forming minerals (Urai *et al.*, 1986; Urai & Jessell, 2001) and whether its mechanical properties will evolve with that recrystallization process.

We have, however, to be careful in interpreting garnet sub-structures, as they can be produced by mechanisms other than creep deformation. Fractures are common in garnet, and may be filled by garnet (precipitating from solution, for example) so that a sub-structure is imposed involving no other phases (Matthews *et al.*, 1992; Prior, 1993; Whitney, 1996). A recent study of eclogitic garnet from the Sesia Zone of the Alps by Trepmann & Stöckhert (2002) is particularly important here as some of the microstructures they described are similar to the microstructures presented in this paper. They interpreted deformation within elongate, asymmetric and sub-structured garnet grains due to cataclasis during seismic loading (a more detailed discussion of this is presented later). It is also true that the presence of garnet sub-structure does not *a priori* necessitate that deformation has occurred. For example, garnet porphyroblasts can develop sub-structures from the amalgamation of many independently nucleated garnet grains (Spiess *et al.*, 2001; Wheeler *et al.*, 2001; Prior *et al.*, 2002; Dobbs *et al.*, 2003) and radial growth structures are observed in some undeformed garnets (Hirsch *et al.*, 2003). Thus, it is important that each sample is assessed on the basis of as much microstructural and micro-chemical data as possible.

This paper advances our understanding of garnet deformation by presenting a study of deformed garnets from Glenelg, NW Scotland.

# TECTONOMETAMORPHIC SETTING

Within the Eastern Unit of the Glenelg–Attadale Inlier of NW Scotland (Fig. 1), eclogites and their retrogressed equivalents are ubiquitous. The eclogites were retrogressed to upper amphibolite-facies assemblages during a period of exhumation related to ductile shearing at this grade. The major shear zones are approximately N–S striking (where not refolded by later structures) and dip moderately to the east. A ~1 km zone of mylonites and ultramylonites demarcates the main structural and metamorphic discontinuity between the Western and Eastern Units, herein termed the Barnhill Shear Zone (BSZ; Fig. 1). A few hundred metres structurally above this shear zone in the Eastern Unit, there is a large (~100 m wide by several hundred metres long) N–S striking rib of eclogite. Within this rib at NG 8055 1570 (Fig. 1) is a thin ~1 m wide, sub-vertical shear zone, striking approximately E–W. The shear zone represents a significant localization of strain as the surrounding eclogites do not contain a mesoscopic fabric. Within the shear zone, garnets form a sub-horizontal penetrative stretching lineation on the foliation surfaces. The matrix comprises very fine-grained amphibole and plagioclase demonstrating that it is a retrograde amphibolite-facies shear zone related to exhumation. This shear zone is cofacial with, and probably temporally related to the BSZ and may represent an anastomosed shear that was localized due
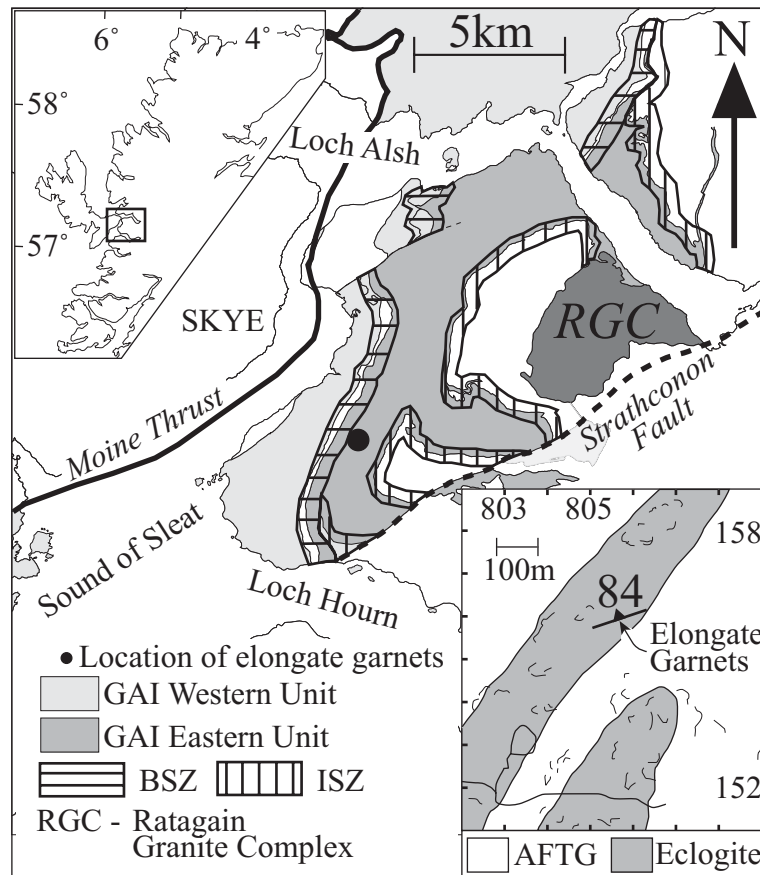
**Fig. 1.** The main map shows the geology of the Glenelg–Attadale Inlier (GAI), modified from Peach *et al.* (1910). The top left inset shows NW Scotland with a rectangle locating the main map. Uncoloured land NW of the Moine Thrust is Torridonian. Uncoloured land SE of the Moine Thrust is Moine. The Barnhill (BSZ) and Inverinate (ISZ) shear zones are marked, as is the location of the sample discussed in this paper. The bottom right inset shows a sketch location map for the elongate garnets and the shear zone containing them (from Storey, 2002). The shear zone foliation is marked. Crag lines and walls are transferred from the Ordnance Survey 1:10 000 sheet and grid numbers are shown. AFTG is amphibole–feldspar trondhjemitic gneiss; eclogite refers to both eclogite and amphibolitized eclogite.

to the rheological properties of the surrounding rigid eclogite body. Amphibole (pargasite) and the feldspar (oligoclase) are identical in composition to the matrix minerals in the major shear zones and to the static retrograde replacement of omphacite and garnet in undeformed eclogites (Storey, 2002).

Thermobarometry has constrained peak temperatures of ~730°C for the eclogites (Sanders, 1989), with peak pressure of ~20 kbar (Rawson *et al.*, 2001; Storey, 2002; Storey *et al.*, 2005). Sanders (1989) demonstrated an early peak isothermal decompression from ~17 kbar to ~15 kbar (i.e. within the eclogite-facies). More recent work has demonstrated that amphibolite-facies retrogression occurred at ~650–700°C and ~13 kbar (Storey, 2002; Storey *et al.*, 2005). Therefore there is strong evidence that there was a pseudo-isothermal decompression of ~20–25 km (~7 kbar) that must have been rapid. Eclogite-facies metamorphism occurred close to 1100 Myr ago (Sanders *et al.*, 1984), whereas the amphibolite-facies retrogression occurred at ~1000 Myr ago (Brewer *et al.*, 2003). Due to the temporal link between the BSZ and the shear zone discussed here, it is probable that similar *P–T* conditions of ~650–700°C and 13 kbar were sustained during shearing. This is certainly compatible with upper amphibolite-facies conditions during shearing, on the basis of both petrographic and *P–T* data.

## ANALYTICAL METHODS
### Electron back-scatter diffraction

The EBSD work presented here was completed during four sessions (1999, 2000, 2002 and 2004) using three different methods. SYTON-polished thin sections (Fynn & Powell, 1979; Lloyd, 1987; Prior *et al.*, 1996) were used throughout. The earliest work comprised

manual EBSD analyses (Prior *et al.*, 1999), located using forescatter orientation contrast images (Prior *et al.*, 1996) on a Phillips XL30 SEM at the University of Liverpool. Analytical details are the same as those used by Spiess *et al.* (2001). All other data were collected using automated EBSD mapping (Adams *et al.*, 1993; Prior *et al.*, 2002) on a CamScan X500 crystal probe, at the University of Liverpool, fitted with a thermionic field emission gun running at 20 keV. Work in 2000 (everything except for the detailed maps of GTS202 and the data on phases other than garnet) was completed at the same time as work published by Prior *et al.* (2002) and uses the same methods. During the EBSD studies conducted from 2002 to 2004, we used a carbon-coated sample and a higher beam current (20 nA); additionally, EBSD patterns were indexed and EBSD maps processed using the Channel 5 software package from HKL Technology and the data were acquired by stitching together several EBSD beam scans. Data were acquired in 2002 (detailed maps of GTS202) at 0·67 s per point and in 2004 (amphibole, feldspar and quartz fabrics) at 0·12–0·18 s per point; increased data acquisition speeds were facilitated by new camera technology and faster computing systems. Error levels for the 2000 work were outlined by Prior *et al.* (2002); the later work has much lower error levels. Map processing procedures have been described by Prior *et al.* (2002).

## Back-scattered electron images and X-ray maps

Most back-scattered electron images (BSE) were collected on a Phillips XL30 SEM, in the University of Liverpool. Further BSE images and X-ray maps were collected on a Cameca SX50 electron microprobe at the University of Leeds, using an accelerating voltage of 20 keV and a beam current of 50 nA. For high-resolution, small-scale X-ray maps we used a beam-scan with a grid spacing of ∼0·065 μm. Lower-resolution, larger maps used a stage-scan, with a grid spacing of 2 μm. In all cases, Ca, Mg and Fe X-rays were collected with a dwell time of 30 ms.

## MICROSTRUCTURAL CONTEXT OF GARNET

Thin sections of the shear zone, cut parallel to the lineation, reveal the intense degree of deformation (Figs 2–4). The sample comprises garnet porphyroclasts and quartz ribbons in a matrix of thoroughly mixed, fine-grained (∼5–10 μm), plagioclase and amphibole (pargasite) with (1–10 μm) relict Na-clinopyroxenes and accessory rutile. Proportions of pyroxene and amphibole vary considerably within individual thin sections. Foliation is defined by garnet porphyroclast shapes (with axial ratios up to about 10:1), quartz ribbon shapes (also with axial ratios up to about 10:1) and millimetre-scale quartz–amphibole/clinopyroxene/plagioclase–garnet layering. Shear bands occur at about 20–30° to the main foliation and always have the same sense of asymmetry. Shear bands are 2–6 mm in length and up to a few hundred micrometres in width. They contain amphibole and/or plagioclase and often small garnet grains and fine quartz ribbons. The amphibole and plagioclase grains are sub-equant and, hence, do not define a tectonic fabric. Quartz ribbons comprise large (200 μm) granoblastic polygons that are almost entirely devoid of undulose extinction. Rutile occurs as stringers of small equant grains within the amphibole–plagioclase matrix.

Quartz ribbons have weak CPOs, as do plagioclase, and amphibole in the matrix (Fig. 2). Clinopyroxene has a well defined non-random CPO, but the symmetry of

**Fig. 2.** Electron back-scattered diffraction (EBSD) data (collected in 2004—see methods) to show the microtextural context of garnet porphyroclasts in the studied sample from Glenelg. The foliation is perpendicular to the plane of the sections and lineation direction is horizontal in the plane of the images. All stereonets are equal-area, and unless stated, lower-hemisphere plots: the reference frame (relative to foliation and lineation) is shown in the centre of the figure. Contouring is based on a counting cone with an opening angle of 15° and contour lines are in multiples of mean uniform density (MUD). Highest point densities are coloured red, lowest point densities blue. Data are plotted as one point for every grain (with grain boundaries defined as ≥10° misorientation), only for grains ≥4 grains times the step-size in diameter. The number of grains and maximum contour values (in MUD) are indicated. (a) EBSD pattern quality map to show the microstructure of quartz ribbons. Step-size is 10 μm. Map is stitched from 10 beam scans. Pale grey ribbons with coarse polygonal structure comprise quartz. Quartz data shown in (f) come from this map. Garnet appears white. The remaining fine-grained material comprises aggregates of pyroxene, plagioclase, amphibole and fine-grained garnet. Rectangle shows the location of the more detailed EBSD map shown in (b). (b) Detailed EBSD map, of the area highlighted in (a), coloured by the phase identified from indexing the diffraction pattern (colour key at bottom left of the map). Step-size is 1 μm. Map is stitched from three beam scans. Garnet, amphibole, clinopyroxene and plagioclase data from this map are shown in (c), (d), (e) and (g). (c) Stereonets (point plots only) to show ⟨100⟩, ⟨110⟩ and ⟨111⟩ garnet orientations from the area mapped in (b). (d) Stereonets (point and contoured data) to show [100], [010] and [001] amphibole orientations from the area mapped in (b). As [010] and [0-10] can be distinguished, [010] is plotted on both upper (UH) and lower (LH) hemispheres (see Brenker *et al.*, 2002). (e) Stereonets (point and contoured data) to show [100], [010] and [001] clinopyroxene orientations from the area mapped in (b). As [010] and [0-10] can be distinguished, [010] is plotted on both upper (UH) and lower (LH) hemispheres (see Brenker *et al.*, 2002). (f) Stereonets (point and contoured data) to show quartz [0001] and ⟨11–20⟩ orientations from the area mapped in (a). As +a and −a can be distinguished, ⟨11–20⟩ (the a-axes) are plotted on both upper (UH) and lower (LH) hemispheres (see Trimby *et al.*, 1998). (g) Stereonets (point and contoured data) to show [100], [010] and [001] plagioclase orientations from the area mapped in (b). As the positive and negative ends of all directions can be distinguished, all are plotted on both upper (UH) and lower (LH) hemispheres (see Prior and Wheeler, 1999). There are significant problems in measuring plagioclase orientations automatically. There is potential for about 10% of the points in this dataset to be wrong, though not enough to upset the overall plagioclase CPO.
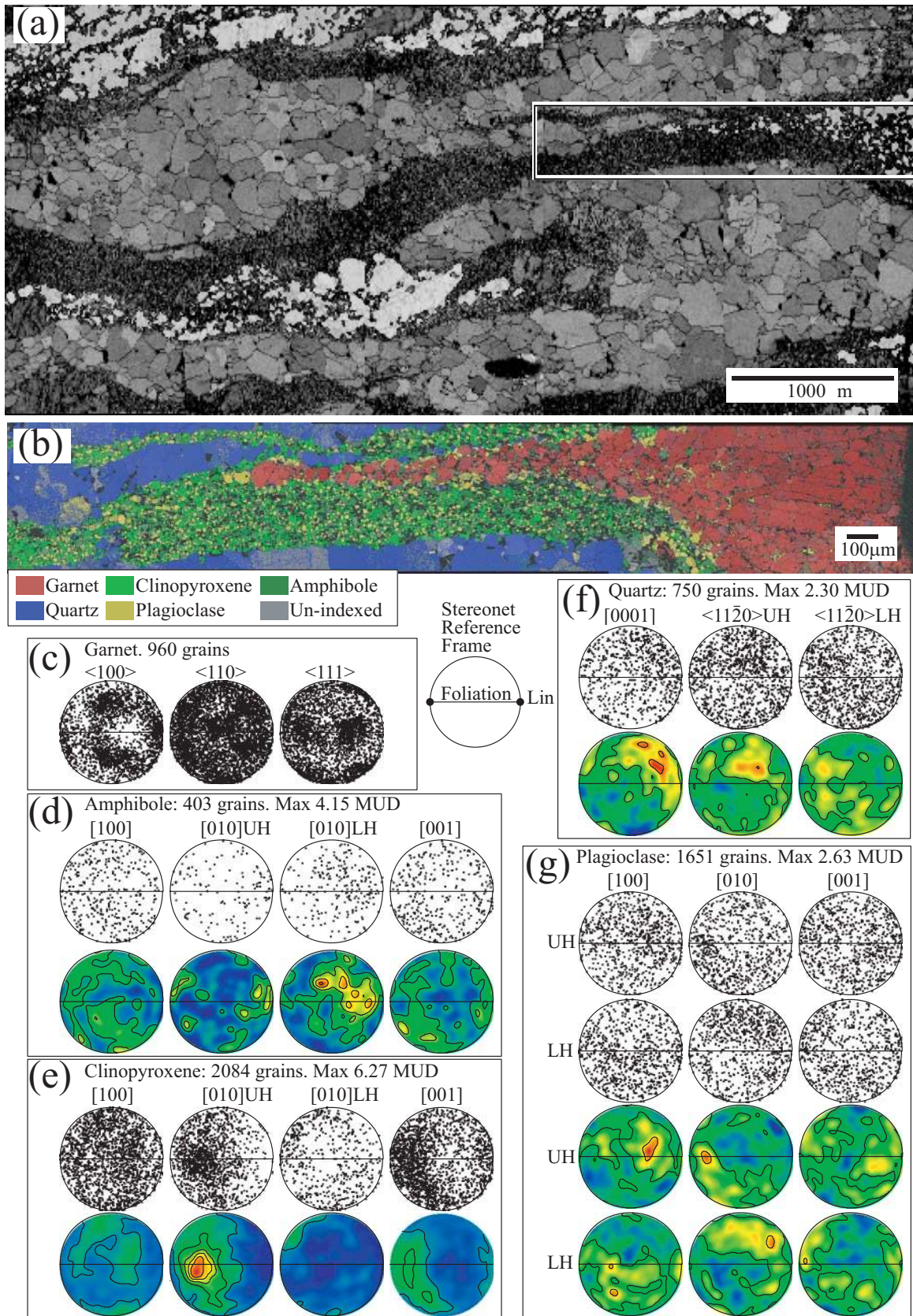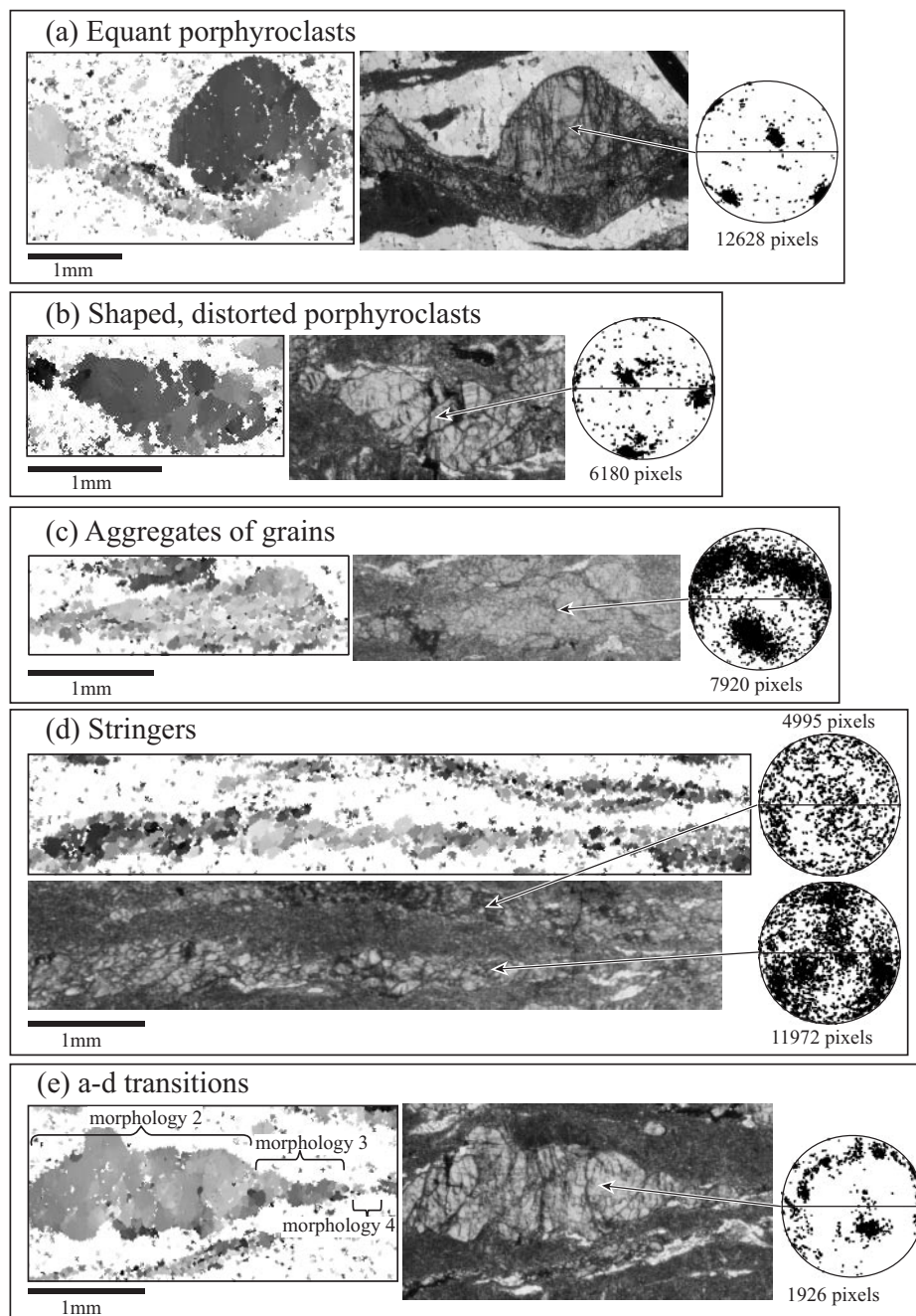
**Fig. 3.** Optical micrographs (right or below) and EBSD maps (left or above), with a 10 μm step-size (data collected in 2000; see Methods), of near end-member porphyroclast morphologies. The foliation is perpendicular to the sections and lineation is horizontal in the plane of the images. The greyscale in the EBSD maps corresponds to one of the Euler angles that define the orientations of each pixel (see Bestmann & Prior, 2003). White pixels have no indexed solutions and generally correspond to phases other than garnet. Accompanying stereonets (lower-hemisphere, equal-area) are all for the ⟨100⟩ direction in garnet and have the same reference frame as the stereonets in Fig. 2. Data for stereonets come from the porphyroclast to which the arrow from the stereonet points. Data are one measurement per pixel on the map. (a) Morphology 1: a large equant porphyroclast (top right) that comprises a single grain with little internal structure. This is wrapped by a second porphyroclast (bottom) of morphology 2 to 3. (b) Morphology 2: shaped porphyroclasts (up to a few millimetres' width) with considerable internal distortion (between fractures), including low-angle boundaries. (c) Morphology 3: shaped porphyroclasts (up to a millimetre's width) that comprise aggregates of many small garnet grains (of about 50 μm diameter) that have some internal deformation. (d) Morphology 4: stringers (generally less than 0·5 mm width) of closely spaced small, idiomorphic garnet grains (of about 50 μm diameter) with intergranular amphibole, plagioclase, pyroxene and quartz. (e) Transitional morphology: a shaped porphyroclast (Morphology 2) of one original parent orientation (Morphology 1) being modified through a thinned zone comprising numerous aggregates of grains (Morphology 3) on the right-hand side of the image, and eventually to a stringer of small idiomorphic garnet grains (Morphology 4) to the far right of the image. A morphology 3–4 porphyroclast lies below this transitional porphyroclast.
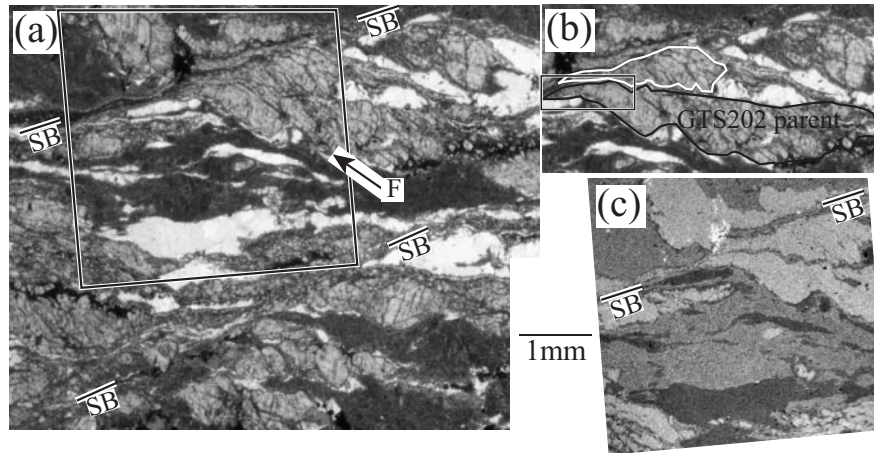
**Fig. 4.** Images of the sample area containing garnet microstructure GTS202. All images are at the same magnification. The foliation is perpendicular to the sections and lineation is horizontal in the plane of the images. Two shear bands (SB) are marked; the upper one affects GTS202. (a) Optical microscope image. The outline shows the area shown in (c). The matrix between the garnet grains comprises aggregates (dark) of fine amphibole and plagioclase and coarse ribbons (white) of quartz. Fractures (F) are deflected into the shear bands. (b) Repeat of top right of (a). The small rectangle shows the area of microstructure GTS202, mapped in detail (Figs 5 and 6). The whole of the parent porphyroclast (identified using EBSD) is outlined with a black line. A neighbouring porphyroclast, also involved in the shearing, is outlined in white. (c) Back-scattered electron (BSE) image of area indicated by the outline in (a), displaying clearly the presence of BSE-bright garnet, BSE-dark quartz and intermediate BSE response amphibole–plagioclase intergrowths.

the CPO does not correspond to the symmetry of the shear zone. Clinopyroxene $\langle b \rangle$-axes are strongly clustered in an orientation significantly oblique to both the lineation and the pole to foliation, $\langle c \rangle$-axes define a weak girdle normal to the $\langle b \rangle$-axis cluster and $\langle a \rangle$-axes are close to random. Although the quartz, amphibole and plagioclase CPOs are weak, they have non-random symmetry elements that are aligned to symmetry elements of the clinopyroxene CPO, but not to the symmetry elements of the shear zone (the foliation and lineation). Clusters of amphibole $\langle b \rangle$-axes, quartz $\langle c \rangle$-axes, and perhaps plagioclase $\langle a \rangle$-axes, align approximately with the clinopyroxene $\langle b \rangle$-axes. Garnet CPOs from the same area are clustered strongly around the orientation of a single porphyroclast that dominates the analysis area. Garnet CPOs will be discussed in more detail later.

## Garnet porphyroclasts

Garnet porphyroclasts vary from equant to elongate. In three dimensions, elongate porphyroclasts are rods. The porphyroclast morphology varies from:

(1) equant large porphyroclasts (up to a few millimetres) that comprise single grains with little internal structure (Fig. 3a);

(2) elongate porphyroclasts (up to a few millimetres wide) with considerable internal distortion (between fractures), including low-angle boundaries (Fig. 3b); CPOs approximate a distorted single crystal (Fig. 3b);

(3) elongate porphyroclasts (up to 1 mm wide) that comprise aggregates of many smaller garnet grains (of about 50 μm diameter) that may have some internal

deformation (Fig. 3c); these small grains are often equant but some are elongate, approximately parallel to the trace of the foliation, with axial ratios up to 2:1 (Fig. 3c); CPOs are scattered widely around a single crystal orientation (Fig. 3c);

(4) stringers (generally less than 0·5 mm wide) of closely spaced small idiomorphic garnet grains (of about 50 μm diameter) with intergranular amphibole, plagioclase, pyroxene and quartz (Fig. 3d); the garnet grains have some internal deformation; these grains are often equant but some are elongate, approximately parallel to the trace of the foliation, with axial ratios up to 2:1 (Fig. 3d); there are also numerous isolated small garnet grains (of about 50 μm diameter) within the amphibole/plagioclase matrix; CPOs are scattered widely around a single crystal orientation (Fig. 3d).

Most garnet porphyroclasts comprise a mixture of more than one of these morphologies (Figs 3e and 4). In a number of cases, porphyroclasts are affected by shear bands (Fig. 4) and there is a transition from morphology 1 to morphology 4 as the shear band is approached. These relationships suggest that the different morphologies are representative of different states of strain of garnet: single crystal porphyroclasts have been deformed to create polycrystalline porphyroclasts. The correspondence of the small grains to high-strain zones suggests that an alternative model in which the small grains amalgamate to create large grains (Spiess *et al.*, 2001) is not viable here.

Fractures of all orientations and varying width are recognized in many, but not all, garnet porphyroclasts.

The fractures have similarities to those described from deformed eclogitic garnets from the Sesia zone (Trepmann & Stöckhert, 2002), although fractures are not as extensive in the Glenelg garnets and most fractures show no shear offset (Fig. 3a). All garnet porphyroclasts of morphologies 1 and 2 have significant intragrain distortion between fractures and the range of shapes cannot be explained by fracture networks alone. Some arrays of spaced fractures have orientations and offsets consistent with their being shear fractures with similar kinematics to the overall shearing (Figs 3c and 4). Where garnet is cut by shear bands, these fractures are deflected into the shear band (Fig. 4) and, in these cases, arrays of more irregular fractures occur perpendicular to, and between, the shear fractures. Fractures are filled with fine-grained aggregates ($\sim$5 μm) of amphibole, plagioclase and quartz. Irregular patches in which grains of these included minerals are slightly larger (5–20 μm) are located in the sites of larger fractures. Probable primary inclusions include rutile–ilmenite grains and relict clinopyroxene, usually surrounded by fine-grained aggregates of amphibole. Rutile inclusions extend along fractures and, in some cases, rutile grains can be traced along fractures to a matrix grain adjacent to the garnet grain boundary.

Below, we present detailed microstructural data from one example (GTS202) of a porphyroclast affected by a shear band and use these data to infer the mechanisms by which the garnet has deformed.

## Microstructure of GTS202

Figure 4 shows the microstructural setting of garnet porphyroclast GTS202; this is one of several garnet grains that are affected by a sinistral shear band oriented about 20° away from the main foliation orientation (Fig. 4a and c). GTS202 is a fragment at the end of a larger parent porphyroclast (Fig. 4b). A series of fractures break up the parent porphyroclast (Fig. 4). GTS202 is about 0·8 × 0·4 mm outside the shear band and is oriented obliquely to both the main foliation and the shear band, the orientation being controlled by the fractures. GTS202 is deflected through 45° and thins to <100 μm as it approaches the shear band. We suggest that this deflection and thinning correspond to an increase in shear strain associated with the shear band. A second porphyroclast, adjacent to the GTS202 parent, undergoes the same shear deformation (Fig. 4b). Stringers of garnet grains (morphology 4) extend into the shear band, from the end of GTS202 and the neighbouring sheared porphyroclast (Fig. 4c). GTS202 shows a transition from a deformed garnet (morphology 1–2) into an aggregate of many smaller garnet grains (morphology 3; Fig. 5) with increasing shear strain. There are considerable sub-structures within GTS202 (Fig. 5).

To facilitate more concise descriptions of the microstructure, we will define terms thus:

(1) low-angle boundaries have misorientations less than 10°, high-angle boundaries have misorientations greater than or equal to 10°; the choice of 10° is arbitrary; we do not think that a more sophisticated approach (e.g. Trimby et al., 1998) will change the conclusions significantly;

(2) the term 'interface' refers to the contact of unlike phases (Sutton & Balluffi, 1995);

(3) grains are regions surrounded entirely by high-angle boundaries and/or interfaces;

(4) grains may contain two or more subgrains; at least part of the boundary between subgrains must be low-angle;

(5) the GTS202 microstructure is divided into three broad areas, as defined in the grain map shown in Fig. 5d; these are called the low-strain area, the transitional area and the high-strain area.

### Boundaries, grains and subgrains

Boundaries and interfaces can be constrained by comparing the BSE image (Fig. 5a), which shows where garnet is present, with the EBSD band contrast image (Fig. 5b), which shows where there are boundaries, and the corresponding boundary map (Fig. 6b) that quantifies misorientation angle across boundaries. The low-strain area of GTS202 approximates a single grain with lattice distortion (Figs 5b–d, 6b and 7a–c) and some low-angle boundaries. Most of the low-strain area of the grain (Fig. 4) is not shown in the detailed maps. EBSD data and orientation contrast images (not shown) indicate that the bulk of this grain (including the right-hand side of the low-strain area shown in the detailed maps Figs 5 and 6) contains no low-angle boundaries—just some discrete changes in orientation that correspond to fractures. The density of boundaries and the misorientations across boundaries increase with increasing strain within the low-strain area (Figs 6b, 7b and c). At the left-hand end of the low-strain area, more low-angle boundaries are developed and define subgrains of about 50 μm in size.

The transitional area comprises a few large 50 to $\sim$200 μm grains containing lattice distortion and 10–50 μm subgrains. The high-strain area of GTS202 comprises individual garnet grains (Figs 5c and 6a) of 10–50 μm diameter, which exhibit lattice distortion and some subgrains (Figs 5b and 6b). The proportion of second phases (quartz, feldspar and amphibole) is higher in the high-strain area (Fig. 5a). Garnet grains in the high-strain area are broadly polygonal. Some of these grains are elongate, approximately parallel to the trace of the foliation, with axial ratios up to about 2:1. High-angle boundaries tend to be straight to gently curved between triple junctions (Figs 5b and 6a) with some
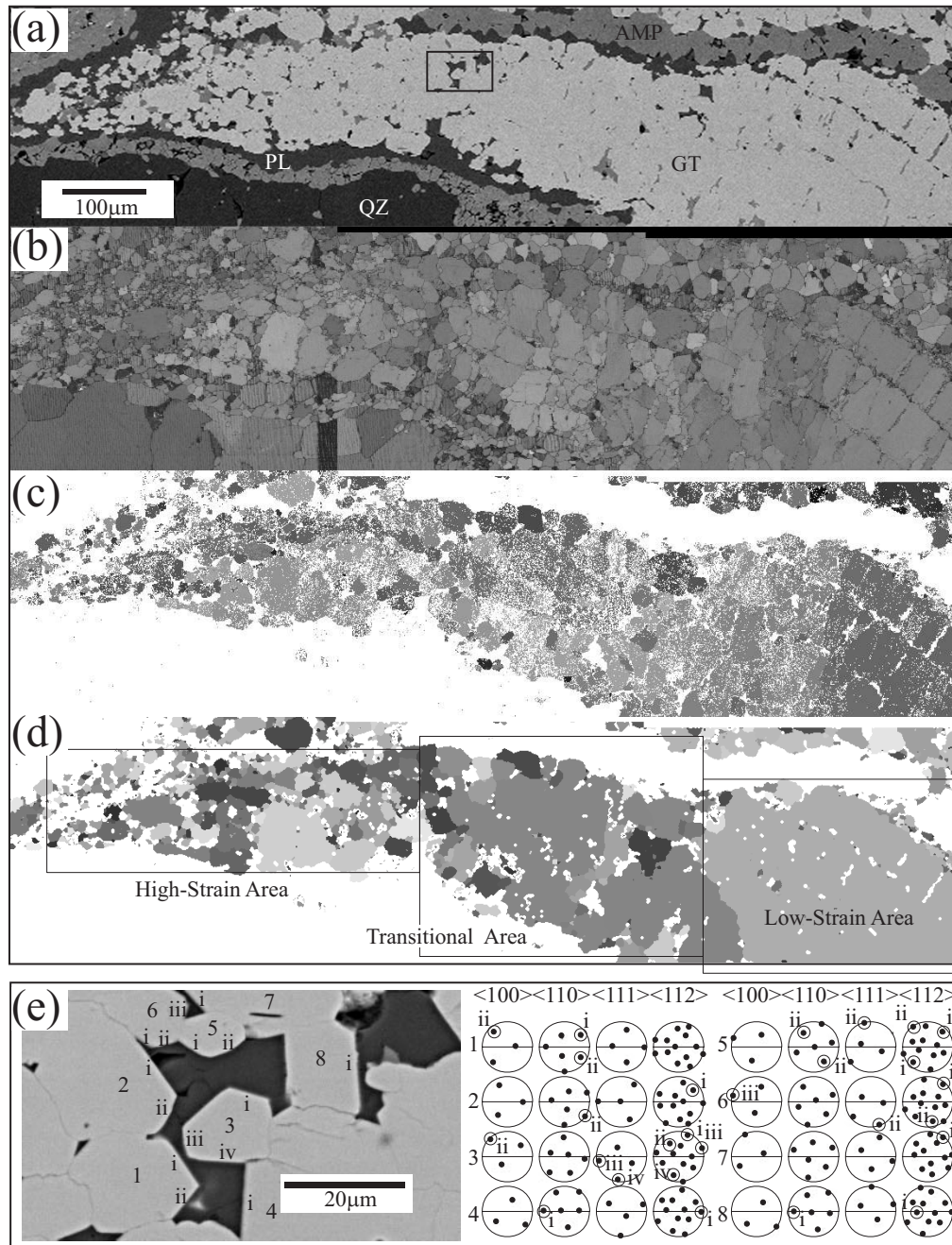
**Fig. 5.** Images of microstructure GTS202. (a)–(d) are at the same scale. All figures are in the same orientation as those in Fig. 4. The shear band cuts the top left of (a)–(d). EBSD data were collected in 2002 (see Methods). The EBSD maps are stitched from three beam scans with a $1\,\mu m$ step-size. (a) BSE image. Rectangle shows area shown in detail in (e). Phases, from brightest to darkest, are: garnet (GT), amphibole/pyroxene (AMP), plagioclase (PL), quartz (QZ). (b) EBSD pattern quality map. The greyscale of each pixel reflects the clarity of the EBSD pattern collected from that point. Pattern quality maps are very similar in their properties to orientation contrast images (Prior *et al.*, 1996). Poor pattern quality (darker) generally corresponds to boundaries and interfaces. (c) EBSD orientation map to show the quality of raw EBSD data. No processing has been applied to these data. Greyscale corresponds to one of the Euler angles that define the orientations of each pixel. White pixels have no indexed solutions and generally correspond to phases other than garnet. (d) Grain map produced from EBSD data. These data have been processed from those shown in (c) to remove probable error pixels and to fill in un-indexed points (see Bestmann & Prior, 2003). Grains are defined by marking all boundaries $>10°$ misorientation and defining domains entirely enclosed by these. Grains are each given different (randomly selected) greyscales. White areas are other phases. The high-strain, low-strain and transitional areas referred to in the text are marked. (e) BSE image to show the nature of interfaces in the transitional–high-strain area. Bright is garnet, dark is plagioclase, intermediate is amphibole. Stereonets (equal-area, lower-hemisphere) show the $\langle 100 \rangle$, $\langle 110 \rangle$, $\langle 111 \rangle$ and $\langle 112 \rangle$ orientations of individual, numbered grains. Crystal directions that are encircled could correspond the trace of crystal faces marked with a corresponding Roman numeral on the BSE image.

irregularity (amplitudes of a few micrometres over wavelengths of a few micrometres; Fig. 5d). Most of these boundaries do not correspond to rational crystallographic planes. In contrast, the garnet interfaces tend to be faceted (Fig. 5a and e). An analysis of the facet traces (Fig. 5e) suggests that most are consistent with being {112} faces, with the remainder {110} faces. {112} and {110} faces are the two most commonly expected in

rhombohedral or icositetrahedral garnets (Read, 1970; Deer *et al.*, 1992).

### Crystallographic preferred orientations and misorientations

The pole figures for GTS202 (Fig. 6c) show a mixed signature. Grains of >200 μm in diameter correspond to the low-strain area and part of the transitional area and these give an orientation close to a single crystal,
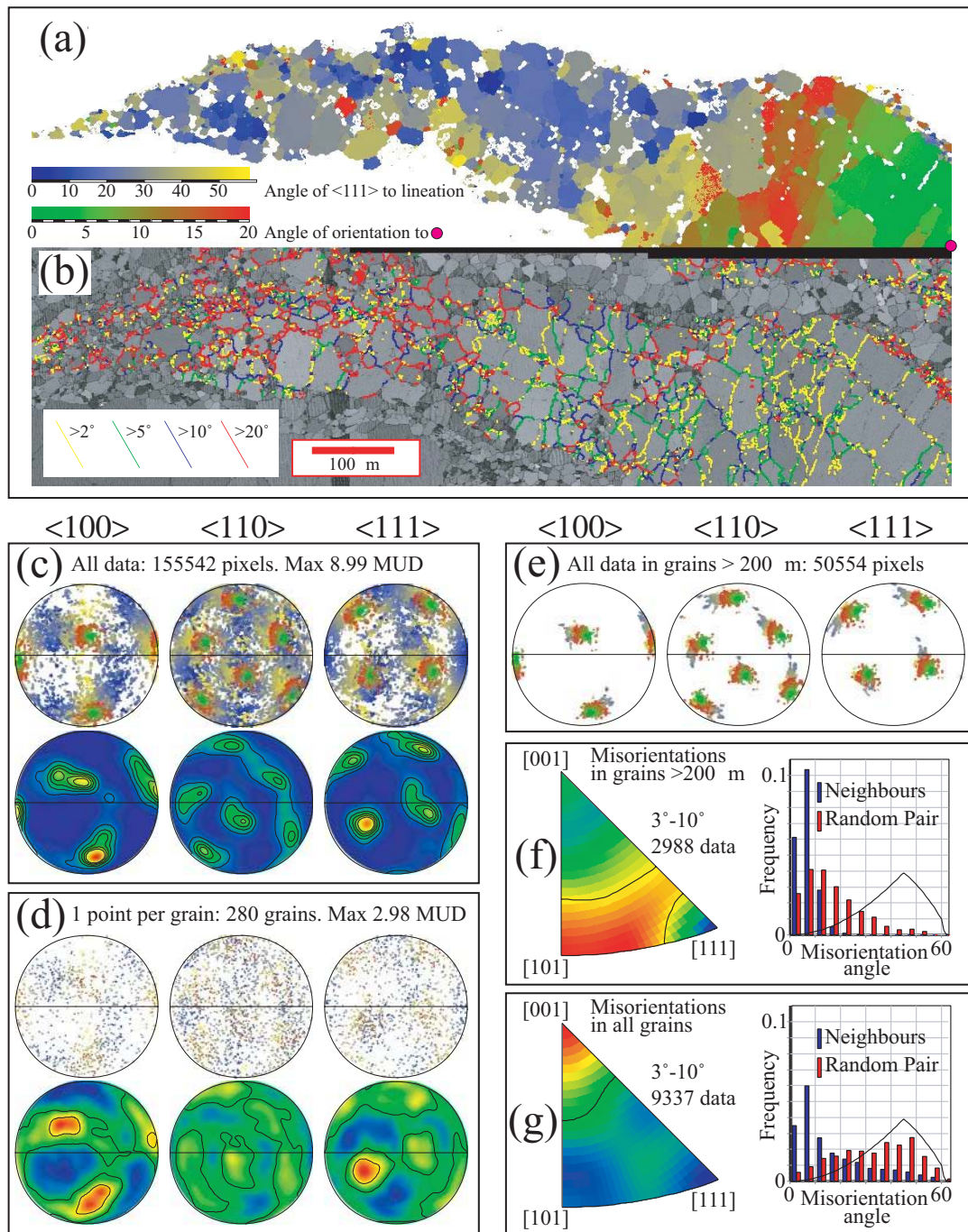
with a rotational dispersion of about 25° around an axis somewhere between the [110] and the [111] on the left side of the pole figure (Fig. 6e). As there are only a few grains in the low-strain and transitional areas, a pole figure in which each grain is represented by one point (Fig. 6d) is dominated by the small garnet grains in the high-strain area. The grains in the high-strain area have orientations (Fig. 6d) that cluster around the preferred orientation of the low-strain area, but contain an extra component of dispersion (25–30°) with no consistent rotation axis.

Orientations along linear transects across the low-strain area (Fig. 7a–c) show a progressive change that corresponds to a dispersion with an anticlockwise rotation around a ⟨110⟩, or perhaps a ⟨111⟩, direction. A transect across the lowest-strain part of the garnet (Fig. 7a), outside the mapped area, shows dispersion around the [110] direction in the bottom left of the pole figure. In transects closer to the transitional area (Fig. 7b–c); the dispersion is around an axis near the [110] and [111] directions that lie closest to the centre of the pole figure (the centre being the kinematic rotation axis of the shear band). Approximately 15° of anticlockwise rotation is accommodated in the low-strain area and a further 10° in the transitional area. Neighbour-pair misorientations (of adjacent pixels) within and between grains of >200 μm in diameter (these are restricted to the low-strain and transitional areas) (Fig. 6f) are dominated by low angles, to the exclusion of angles of >20°. These low angles are represented in the random-pair distribution but are not as significant, suggesting that neighbouring pixels have a tendency towards low-angle misorientations that is not merely a function of the strong preferred orientation (Wheeler *et al.*, 2001). Neighbour-pair misorientation axes in the low-strain and transitional areas show a preferred orientation parallel to the ⟨110⟩ direction (Fig. 6f) for misorientations <10°, consistent with the transect data shown in Fig. 7.

Linear transects that cross from the transitional area into the high-strain area (Fig. 7d) show discrete changes in orientation corresponding to boundaries and a loss of the crystallographic control on dispersion as the high-strain area is entered. High-angle grain boundaries (dominantly in the high-strain area) have random misorientation axes (Fig. 8). Neighbour-pair misorientations for the whole dataset show a tail of high-angle misorientations superposed on the low-angle misorientations (Fig. 6g). As no misorientations of >20° are apparent in lower-strain areas (Fig. 6f), the tail of high-angle misorientations must relate to the high-strain area. Neighbour-pair misorientation axes for misorientations of <10° in the whole sample are generally parallel to ⟨100⟩ directions (Fig. 6g). As the low-strain and transitional area misorientation axes are ⟨110⟩ dominated, the ⟨100⟩ misorientation axes must be developed in the high-strain area: grains in the high-strain area have internal distortions and subgrains with ⟨100⟩ misorientation axes.

### Compositional data

Back-scattered electron images do not display any clear chemical heterogeneities within the garnet (Fig. 5), so X-ray maps of Ca, Mg and Fe were taken from critical areas to investigate this further. In all cases, the chemical variation is most prominent for Ca. Mg and Fe display antithetic relationships to Ca but with a weaker X-ray signal; hence, all X-ray maps discussed are for Ca (Fig. 9).

Chemical zoning of garnet is only significant in the transitional and high-strain area. A clear chemical substructure correlates strongly with the locations of garnet boundaries (Fig. 9). Ca-lows occur along most of the boundaries and are equally well developed on low-angle (e.g. between subdomains 5 and 6, and 7 and 8; Fig. 9) and high-angle (e.g. between subdomains 1 and 4, 2 and 3, and 9 and 10; Fig. 9) boundaries. However, the most spectacular features of the X-ray maps are the Ca-highs that occur along some high-angle boundaries, as discrete

**Fig. 6.** EBSD maps and data from microstructure GTS202. These data, collected in 2002 (see Methods), have been processed from those shown in Fig. 5c to remove probable error pixels and to fill in un-indexed points (see Bestmann & Prior, 2003). Stereonets have the same reference frame as Fig. 2. Stereonets in (c), (d) and (e) are equal-area, lower-hemisphere plots. Inverse pole figures in (f) and (g) are upper-hemisphere plots. Contouring is based on a counting cone with an opening angle of 15° and contour lines are in multiples of mean uniform density (MUD). In contoured stereonets, highest-point densities are coloured red, lowest-point densities blue. Colours in the point data correspond to colours in the EBSD map (a). The number of grains or pixels and maximum contour values (in MUD) are indicated. (a) EBSD map to show the source of data for (c)–(g). Only data from garnet that is clearly part of a single porphyroclast (coloured here) are used: compare this map with Fig. 5d to see which data from the original map have been excluded. Garnet that is misoriented by less than 20° from a point in the bottom right (red circle) is coloured according to the misorientation relative to that point. All other garnet is coloured according to the angle between the lineation and ⟨111⟩. (b) Boundary map (all misorientations calculated between neighbouring pixels) superposed on EBSD pattern quality map; compare with Fig 5b. (c) Stereonets (point data above, contoured below) to show CPO that corresponds to the map in (a). Every coloured pixel in (a) is plotted, so that the contoured plot is weighted by the area fraction of orientations. (d) Stereonets (point data above, contoured below) showing the same dataset as (c) but data are plotted as one point for every grain (with grain boundaries defined as ≥10° misorientation (see (b) and Fig. 5d), only for grains ≥4 grains times the step-size in diameter. (e) Stereonets (point data only) to show the same dataset as (c) picked for grains over 200 μm in diameter. The plot contains only data from the low-strain and transitional areas. (f) Misorientation data from GTS202 for grains >200 μm, corresponding to the data plotted in (e). Misorientation angles are plotted as frequency histograms for neighbour pairs and random pairs (Wheeler *et al.*, 2001). The line superposed on each histogram shows the expected misorientation distribution for a random CPO. Misorientation axis data for low-angle boundaries (misorientations between 3° and 10°) are plotted in an inverse pole figure. (g) Misorientation data from GTS202 for all grains, corresponding to the data plotted in (c). See (f) for details.
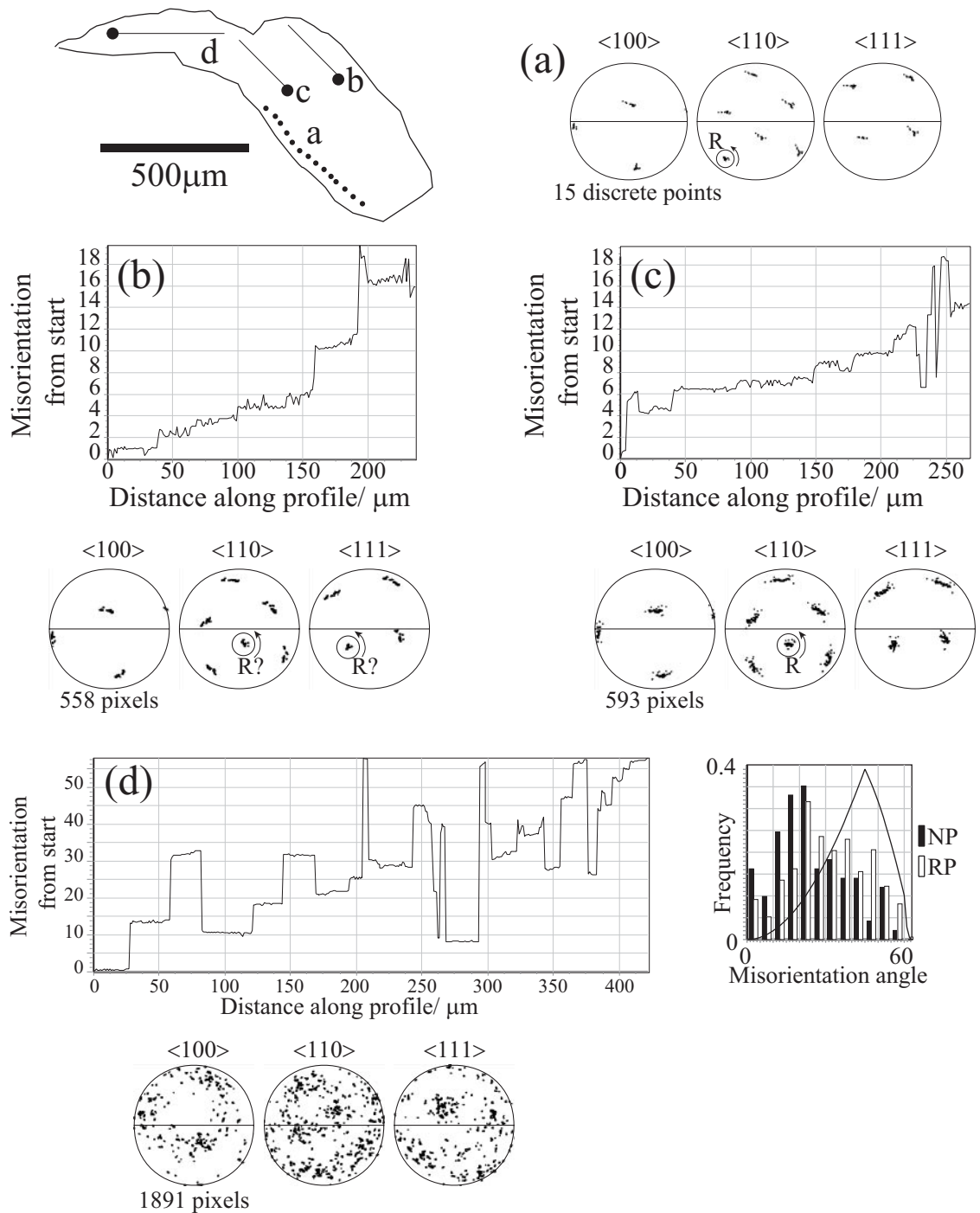
**Fig. 7.** Profiles of misorientation along transects within GTS202 and accompanying stereonets. Transect (a) represents EBSD data points collected manually (in 1999, see Methods): the transect is marked as a series of dots, each representing a data point. Transects (b)–(d) represent EBSD data collected automatically (2002): data are extracted from those shown in Figs 5 and 6 along chosen lines. These transects are marked as a continuous line, with the start point from the dot annotated with the transect label. Stereonets (lower-hemisphere, equal-area) have the same reference frame as stereonets in Fig. 2. Where there are rotation axes that can explain the dispersion of data, these are marked with a circle labelled 'R'. Senses of rotation along transects, where they are consistent, are marked with an arrow. (a) Stereonets showing discrete measurements that define a transect across the low-strain area. (b) Misorientation transect within the low-strain area; corresponding stereonets are below transect. (c) Misorientation transect within the low-strain area, just entering transitional area; corresponding stereonets are below transect. (d) Misorientation transect within the high-strain and transitional areas; corresponding stereonets are below transect. Misorientation data are plotted to the right of the transect: misorientation angles for this line dataset are plotted as frequency histograms for neighbour pairs (NP) and random pairs (RP) (Wheeler *et al.*, 2001). The line superposed on each histogram shows the expected misorientation distribution for a random CPO.
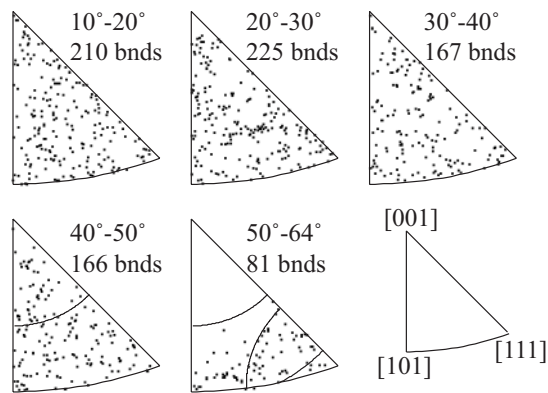
**Fig. 8.** Equal-area, upper-hemisphere inverse pole figures (IPFs) to show the misorientation axes for high-angle boundaries. Data are plotted as one point per boundary, for all boundaries ≥10° misorientation, from the EBSD data shown in Fig. 6a. The data are divided into five bins based on misorientation angle (10°–20°, 20°–30°, 30°–40°, 40°–50° and 50°–64°) and these are shown as five separate IPFs. The number of boundaries (bnds) plotted on each IPF is stated. Forbidden zones (see Wheeler *et al.*, 2001) are shown in the 40°–50° and 50°–64° plots. IPF at the bottom right locates the [001], [101] and [111] axes.

patches adjacent to the boundaries. In the transitional area, at least two linear tracts of Ca-rich garnet (one including the boundary of subdomains 10 and 11 and the other including the boundary of subdomains 12 and 13) are oriented sub-perpendicular to the overall garnet long axis (Fig. 9f). Neither extends across the entire width of the garnet and both are associated with high-angle boundaries and/or interfaces. The boundaries are located within the high-Ca tracts rather than next to them. In the high-strain area, individual, elongate garnet grains (e.g. subdomains 1 and 2; Fig. 9) are zoned so that Ca-highs are developed preferentially on the boundaries or interfaces parallel to the short axis (Fig. 9c). A thin Ca-low, similar to that on most boundaries, occurs along relatively sharp lines that juxtapose cores of these grains and their Ca-rich ends. Generally, there is no crystallographic boundary corresponding to these changes in chemistry and where there is a boundary, it is low-angle. The Ca-highs are developed best, although not exclusively, at interfaces (most noticeably against quartz) and the Ca-rich garnet has well-developed facets at the interface. In another high-strain area, not covered by the detailed EBSD maps, discrete garnet grains have Ca-low rims and a 'pore-filling' network of Ca-rich garnet (Fig. 10). Garnet grains with Ca-highs are elongate. The Ca-low parts of these grains (e.g. subdomains 1 and 2 in Fig. 9) are also commonly elongate.

## Bulk CPO

Measuring the bulk CPO of garnet in this sample by EBSD is not easy. A single thin section contains no more than 50 or so porphyroclasts. These show no preferred orientation; the small number of porphyroclasts analysed renders the result statistically insignificant. Measuring the bulk CPO of small garnet grains, developed in morphologies 3 and 4 (e.g. the high-strain area of GTS202) is more feasible. Figure 11 shows the CPOs of 17 individual porphyroclasts from one thin section. The data from each porphyroclast are plotted as one point per grain, so that a small grain is given as much weighting as a large one; the effect of this can been seen in data for GTS202, which are plotted as one point per grain in Fig. 6d. The datasets from all the porphyroclasts have been added together and the overall result (Fig. 11b) is a weaker CPO than that shown by any individual porphyroclast. The bulk CPO is still not random, however—each porphyroclast dataset clusters around a single crystal orientation and with only 17 porphyroclasts in the bulk CPO, there is still a weak single crystal signature that is biased by the most significant individual porphyroclast dataset. The bulk CPO does have some similarities to measured and modelled simple shear fabrics (Mainprice *et al.*, 2004). However, it is dominantly a single crystal signature and it seems reasonable that the weak CPO is an artefact of poor statistics. We believe that a statistically more significant dataset is likely to show a random CPO.

## Deformation, recovery and recrystallization mechanisms

### Dislocation creep and recovery

Dispersions with rational crystallographic rotation axes, as seen in porphyroclast morphologies 1–2, are a clear indicator of plastic deformation by dislocation creep (Lloyd & Freeman, 1991; Lloyd *et al.*, 1997; Boyle *et al.*, 1998; Prior *et al.*, 2002; Bestmann & Prior, 2003). In GTS202, the sense of dispersion (anticlockwise rotation), with increasing strain, is consistent with the sinistral kinematics of the shear band and the amount of rotation in the low-strain and transitional areas is of the same order as the amount of bending of the porphyroclast margin in the same areas. Thus, it seems reasonable that dislocation creep deformation of garnet was due to larger-scale shearing.

Low-angle boundaries that share the same dispersion geometry suggest that recovery has accompanied plastic deformation. Some, but not all, low-angle boundaries correspond to fractures, indicating that fracture and plastic deformation maybe closely linked (see Trepmann & Stöckhert, 2002). However, the dominance of non-fracture low-angle boundaries in GTS202 and the intra-subgrain distortion suggest that dislocation creep and recovery are the most important processes in the development of garnet subgrains. Similar microstructures have been described recently in other garnet samples (Prior *et al.*, 1999, 2000, 2002).
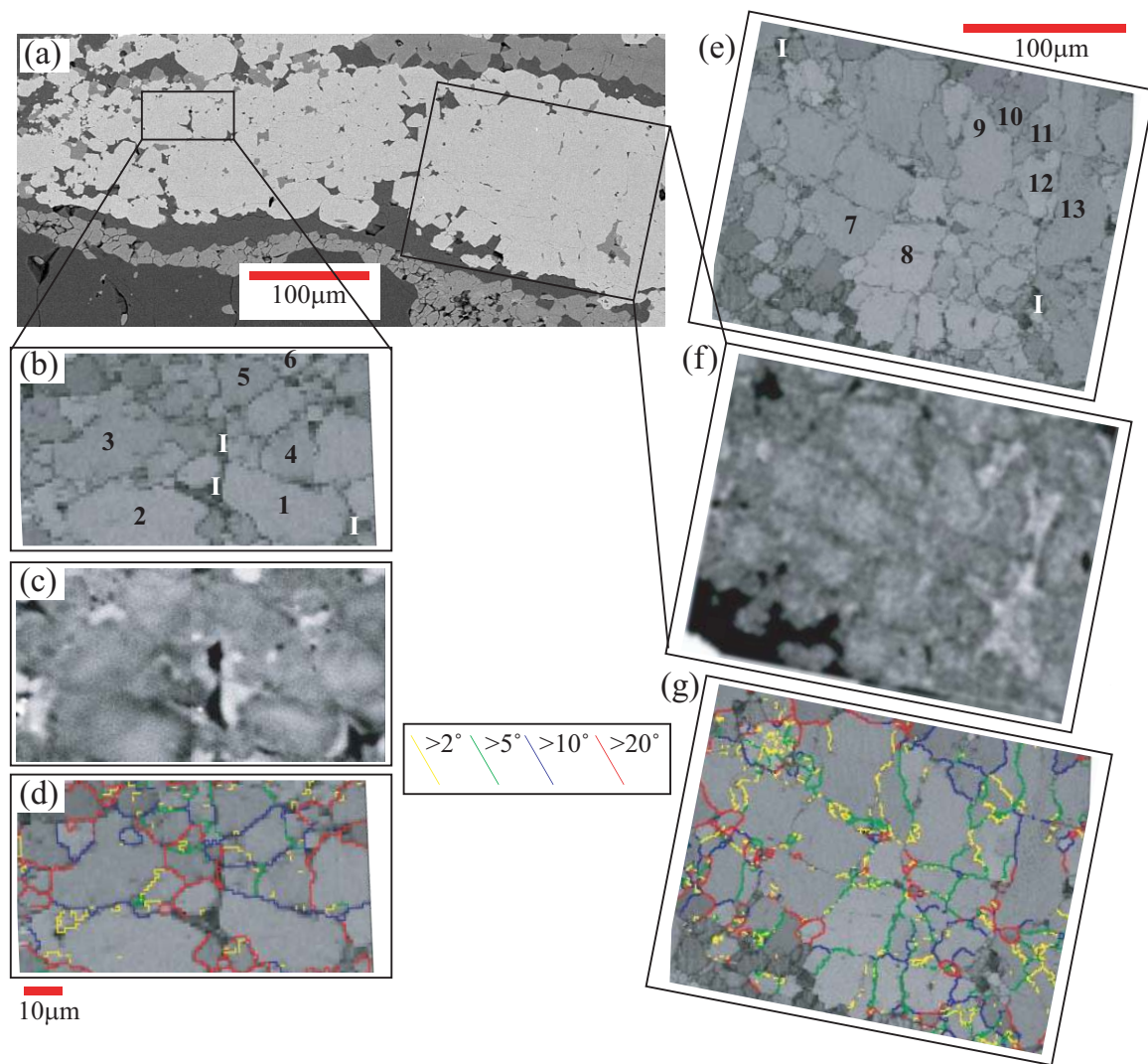
**Fig. 9.** Maps from the high-strain and transitional areas, to compare crystallographic data with compositional data. (a) Back-scattered electron image; the boxes locate more detailed maps (b)–(d) and (e)–(g). The scale bar for (b)–(d) is shown below (d). The scale bar for (e)–(g) is shown above (e). (b) EBSD pattern quality map (extracted from data shown in Figs 5 and 6) of part of the high-strain area; shown by the left-hand rectangle in (a). Boundaries correspond to lower (darker) pattern quality. The positions of non-garnet phases are marked with a white I. Grain numbers are referred to in the description in the text. (c) Small-scale (high-resolution beam scan) Ca X-ray map of the same area as shown in (b). Lighter shades indicate greater Ca content. (d), as (b), with misorientation boundaries, coloured according to misorientation, superposed. (e), as (b), but of part of the transitional area; shown by the right-hand rectangle in (a). (f) Large-scale (low-resolution, stage-scan) Ca X-ray map of the same area as shown in (e). Lighter shades indicate greater Ca-content. Grain numbers are referred to in the description in the text. Some of the Ca-high areas (e.g. below grains 12 and 13; see (e)) correspond to amphibole but most (e.g. between grains 12 and 13, between grains 10 and 11) occur within garnet sufficiently far from interfaces ($\gg$ the few micrometres activation volume) that they must reflect the garnet composition. (g), as (e), with misorientation boundaries, coloured according to misorientation, superposed.

The dispersion geometry can be inverted to constrain the dislocation systems that accommodate plastic deformation and make up subgrain walls: in one garnet from this sample, dispersions around $\langle 110 \rangle$ are best explained by slip on dislocations with Burgers vectors $1/2 \langle 111 \rangle$ (Prior *et al.*, 2002). The low-strain and transitional areas of GTS202 are also dominated by dispersions around $\langle 110 \rangle$, with the most probable boundary planes $\{111\}$. These data are also consistent with slip on $1/2\langle 111 \rangle$. The larger dataset shows a range of dispersion axes, dependent presumably upon the grain orientation and the potential for slip on different dislocation systems. The development of significant $\langle 100 \rangle$ misorientations on low-angle boundaries in the high-strain area of GTS202 may reflect the activation of different slip systems as the grain orientation changes. This aspect warrants further work but will not be explored further here.
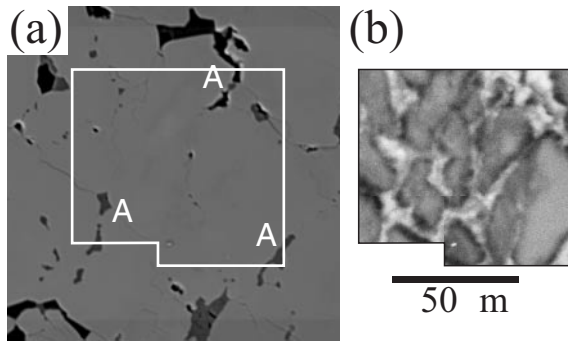
**Fig. 10.** Maps from a high-strain area located ∼150 μm above the GTS202 microstructure. The area is located above the box marked in Fig. 4b, very close to the shear band and within the neighbouring porphyroclast (outlined in white in Fig. 4b). (a) Back-scattered electron image. Amphiboles (dark) are marked with an A. Box shows precise location of (b). (b) Ca X-ray map (stitched from four high-resolution beam scans) of the area boxed in (a). Lighter shades indicate greater Ca-content.

### Subgrain/grain boundary segregation

Ca-lows are observed on many boundaries. We will argue later that the Ca-highs represent the stable garnet composition that grew during deformation. Although it is tempting to suggest that the Ca-lows relate to diffusion along grain and subgrain boundaries, this idea is inconsistent with the high-Ca garnet being the stable composition. An alternative explanation is that the Ca-lows represent segregation along subgrain or grain boundaries such as that commonly observed in metallic alloys, semiconductors and ceramics (Bernardini, 1998; Ross *et al.*, 2001; Wynblatt *et al.*, 2003). Individual dislocations distort the lattice. In a solid solution such as garnet, the distorted lattice around the dislocation may have dimensions that match one solid-solution end-member better than the others. Short-range vacancy diffusion, to increase the concentration of that end-member in the distorted region, will reduce the stresses related to these dislocations. The process does not require long-range lattice diffusion to concentrate the favoured end-member along a subgrain boundary, as the diffusion will be facilitated by dislocation climb during recovery. As we suggest that subgrain boundaries develop into grain boundaries by rotation recrystallization (see below), the grain boundaries will inherit the subgrain boundary composition. These ideas must remain speculative at the moment—the level of detail needed to firm up these ideas is well beyond the scope of this work.

### Generation of new grains: subgrain rotation recrystallization

The increase in low-angle boundary density and misorientation as the strain increases in the low-strain area suggests that subgrain rotation (White, 1977; Poirier &

Guillope, 1979) has operated in conjunction with recovery (see definitions in Trimby *et al.*, 1998). The observation that garnet grains in the high-strain area have similar sizes to the subgrains in the neighbouring transitional area is consistent with the grains having developed by subgrain rotation recrystallization (Poirier & Guillope, 1979).

### Grain boundary sliding

The random dispersion of the orientations of grains in high-strain areas around the orientation of garnet in the low-strain area of the same porphyroclast can be achieved by grain boundary sliding and concomitant grain rotations that have no crystallographic control (Jiang *et al.*, 2000; Bestmann & Prior, 2003). Ultimately, this would lead to the randomization of the garnet bulk CPO as the data presented in Fig. 11 suggest.

Grain boundary sliding would be consistent with the increasing proportion of second phases, incorporated into garnet porphyroclasts, with increasing strain as grain boundary sliding necessitates neighbour switching (Ashby & Verrall, 1973; Boullier & Gueguen, 1975; Drury & Humphreys, 1988; Fliervoet *et al.*, 1997) and can facilitate mechanical mixing of garnet grains with amphibole, pyroxene, quartz and feldspar in neighbouring layers. This process requires that the other phases also deform by a sliding mechanism. It is notable that the other phases do not have CPOs that correspond to the shear zone kinematics. We suggest that the CPOs that are observed in pyroxene, quartz, amphibole and plagioclase pre-date shear zone deformation. These CPOs have been weakened but not destroyed by a randomization process associated with grain boundary sliding (see Jiang *et al.*, 2000).

Grain boundary sliding, accommodated by diffusion, has been suggested as an explanation of garnet microstructures in eclogite-facies shear zones (Terry & Heidelbach, 2004). In our study, it is clear that grain boundary sliding did not operate to the exclusion of other mechanisms. There is evidence that grains continued to deform internally by dislocation creep.

### Diffusion creep

Grain boundary sliding needs an accommodation mechanism. Mechanisms include frictional sliding and associated dilatation (Sammis, 2001; Bocquet *et al.*, 2002; Shodja & Nezami, 2003), diffusion creep (Ashby & Verrall, 1973; Gifkins, 1973, 1976) and grain boundary dislocation creep (Gifkins, 1991, 1994). Randomization of garnet orientations around porphyroclasts from the Sesia zone (Trepmann & Stöckhert, 2002) is postulated to occur by a cataclastic (frictional) process: Trepmann & Stöckhert (2002) show good evidence (their figs 4a and 7) that the shapes and size distributions of small
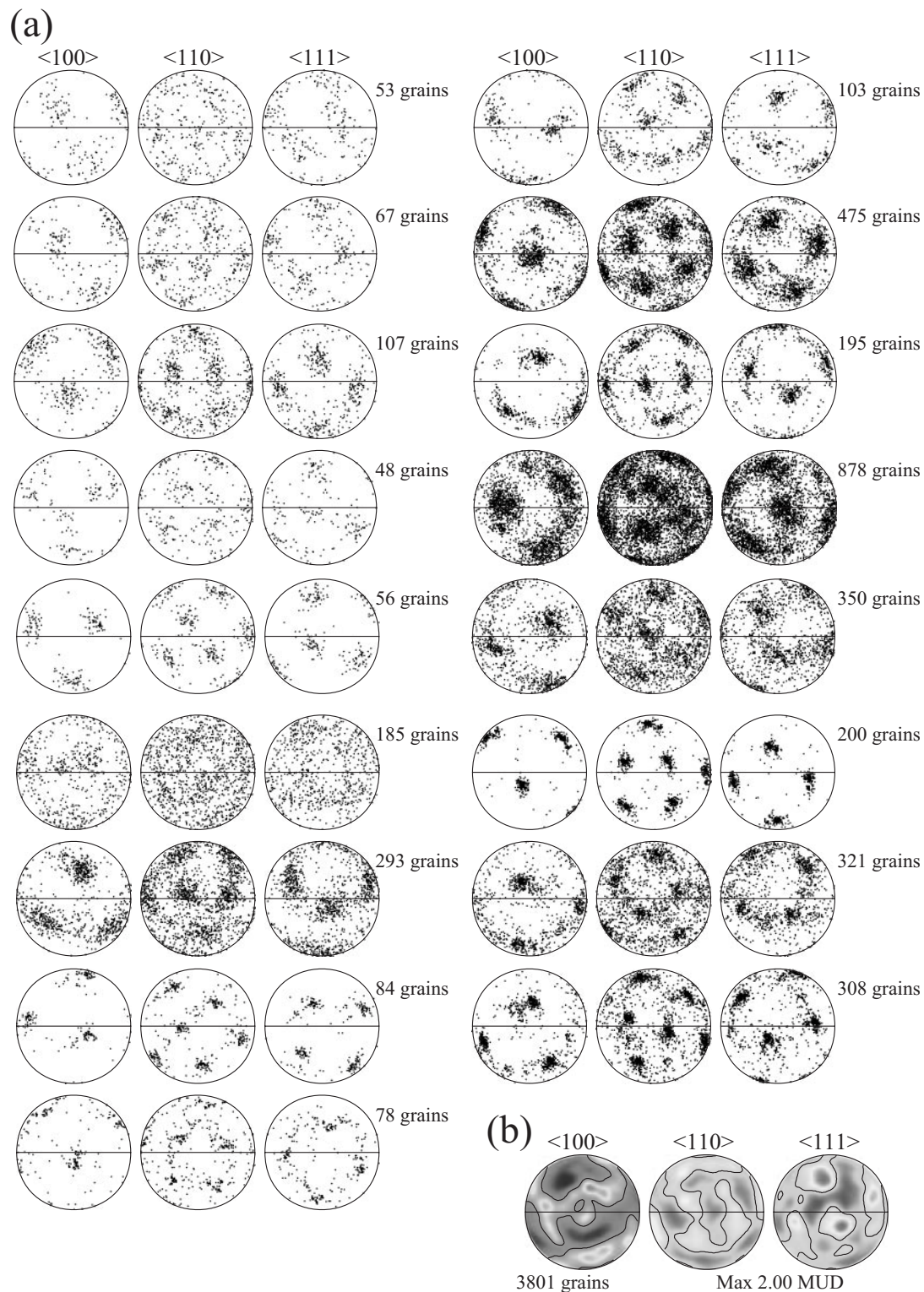
**Fig. 11.** Garnet crystallographic preferred orientation (CPO) data. All stereonets are equal-area, lower-hemisphere plots. Reference frames are the same as those shown in Fig. 2. (a) Data from 17 individual garnet porphyroclasts. For each porphyroclast, the $\langle 100 \rangle$, $\langle 110 \rangle$ and $\langle 111 \rangle$ directions are plotted. Data are plotted as one point for every grain (with grain boundaries defined as $\geq 10°$ misorientation), only for grains $\geq 4$ grains times the step-size in diameter. (b) All the data in (a) combined and contoured. Contouring is based on a counting cone with an opening angle of 15° and contour lines are in multiples of mean uniform density. The maximum intensity is shown.

garnets relate to fractures. Such evidence is lacking here and, as discussed above, the generation of small garnet grains in high-strain areas is best explained by subgrain rotation recrystallization. Ca-rich garnet provides the best evidence to suggest that diffusion was an important process during garnet deformation. The interfaces of Ca-rich garnet are well faceted. Dissolution can create facets, but on a smaller scale than the grains being dissolved (Prior, 1993). Idiomorphic crystal forms observed here, where facet dimensions are the same order as grain-size, are best related to growth of these surfaces (see discussion by Spiess *et al.*, 2001). Garnet growth requires diffusion. Ca-rich garnet overgrowths are developed adjacent to some high-angle boundaries—most specifically, high-angle boundaries that would have been in an extensional orientation with respect to the shear zone kinematics. One way to explain this would be the growth of garnet in opening void spaces during deformation.

There is good evidence for diffusion. The relationship of Ca-rich garnet to extensional sites suggests that this diffusion operated during deformation and that diffusion creep provides the most probable mechanism to control the grain boundary sliding process. Furthermore, the preservation of zoning profiles within individual garnet grains and the correspondence of chemical heterogeneities to boundaries suggest that grain boundary diffusion (Coble creep, pressure solution) was more likely than volume diffusion. Volume diffusion would be unlikely to be a kinetically favourable process at the temperatures of deformation here (Yardley, 1977; Ayres & Vance, 1997).

The morphology of garnet triple junctions that contain second phases (Fig. 5e) is reminiscent of microstructures that indicate the presence of melt (D. Kohlstedt, personal communication; see Mei *et al.*, 2002). Whether melt is present or not, a mechanism is still required for boundary sliding. The presence of melt has not been suggested by any of the detailed petrological or geochemical studies of the Glenelg eclogite described here (Sanders, 1988, 1989; Storey, 2002). Triple junctions generally contain single-phase inclusions that have similar dimensions to the grains of the same phase in layers outside the garnet. Triple junction geometries may be due simply to the impingement of faceted garnet interfaces around second-phase inclusions (Elliott *et al.*, 1997; Holness *et al.*, 2005) and do not necessitate that these inclusions were melt.

### The role of fracture

The garnet porphyroclasts are clearly fractured and some fractures are kinematically linked to the shearing. They contain minerals that suggest that they formed at the same conditions as the plastic deformation of the garnet. Trepmann & Stöckhert (2002) suggested, for Sesia Zone garnets, that some fractures are developed along pre-existing low-angle grain boundaries and we cannot rule

this out in the Glenelg garnets. However, the bending of fractures into shear zones, coupled with the plastic deformation of the garnet that forms the fracture walls, suggests that some fractures pre-date some of the plastic shearing. One suggestion is that fractures relate to decompression from eclogite to lower pressures (G. Cressey, personal communication). Given the kinematic links, it seems probable that fracturing and plastic deformation were broadly synchronous. This is an issue that warrants further investigation and is beyond the scope of this paper. Trepmann & Stöckhert (2002) have suggested that such fractures could represent a response to deep crustal seismic events. If this is true here, then the plastic deformation may correspond to pre-seismic stress build-up and post-seismic relaxation. Alternatively, the fractures may be sub-critical (Prior, 1993), and may accommodate deformation aseismically, essentially by processes that involve diffusion.

## CONCEPTUAL MODEL

We present here a conceptual model that explains best the data presented in this paper. The original garnet porphyroclasts are relics of the earlier eclogite-facies metamorphism. Deformation occurs in the amphibolite facies. Although most of the deformation is accommodated by fine-grained aggregates of amphibole, pyroxene, feldspar and quartz, significant garnet deformation also occurs. Garnet porphyroclasts evolve from morphology 1 to morphology 4 (as defined earlier; Fig. 3) during progressive deformation.

(1) Original garnet grains (morphology 1) deform by dislocation creep (Fig. 12a, stage 2–3); fractures form either before, or synchronously with, plastic deformation.

(2) The garnet recovers (probably dynamically) and subgrain rotation occurs (Fig. 12a, stage 4) to give sub-structured porphyroclasts (morphology 2); 'segregation' occurs, probably as part of the recovery process, to fix garnet of a different composition along subgrain boundaries.

(3) Dislocation creep and recovery (i and ii) disperse garnet crystallographic orientations around rational crystallographic axes (Fig. 12c, stage 2–4).

(4) Subgrain rotation recrystallization creates small garnet grains (morphology 3), from pre-existing subgrains (Fig. 12a, stage 5; Fig. 12d); the new grain boundaries preserve their Ca-low composition.

(5) High-angle boundaries are able to slide; the sliding facilitates granular flow that weakens the CPO by random dispersion (Fig. 12c, stage 5; Fig. 12d).

(6) Grain boundary sliding is accommodated primarily by diffusion; void spaces open up along suitably oriented boundaries (Fig. 12d); garnet of a different composition (higher Ca-content) grows into the void
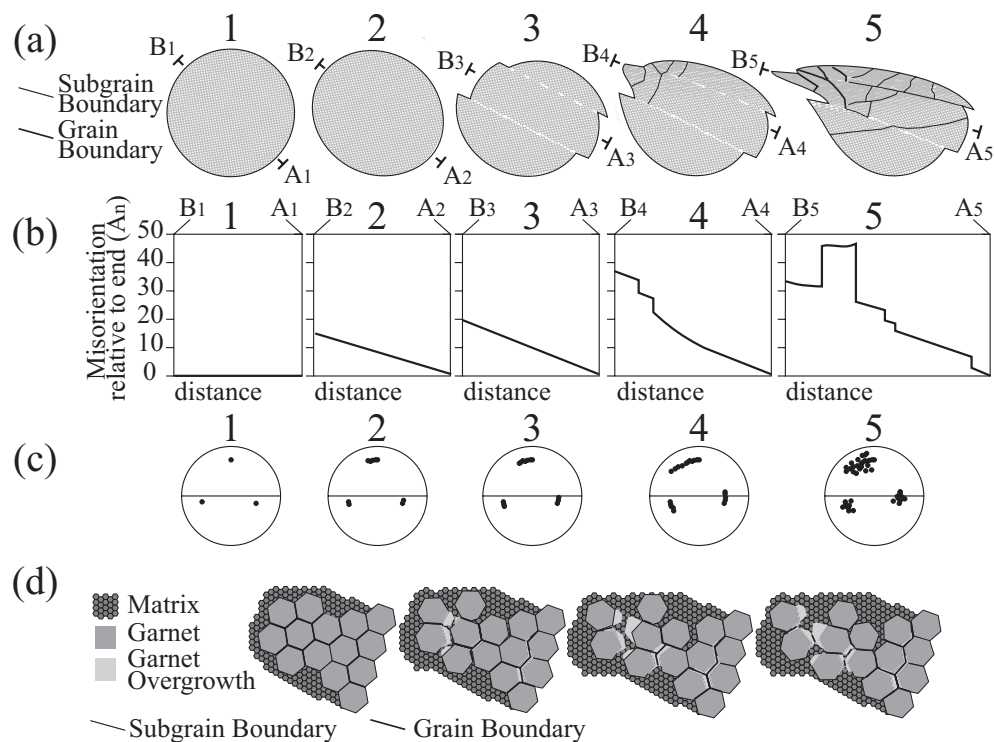
**Fig. 12.** Schematic illustration of the evolution of the microstructure and CPO of a garnet porphyroclast. (a)–(c) are divided into five time stages (1 to 5). (d) represents the details in time stage 5. (a) Porphyroclast shape and sub-structure. Stage 1 undeformed, stage 2 plastically distorted lattice, stage 3 some fractures and more distortion, stage 4 recovery, stage 5 subgrain rotation recrystallization. Misorientation profiles ($A_1$ to $B_1$, $A_2$ to $B_2$, etc.) shown in (b) are marked. (b) Misorientation profiles ($A_1$ to $B_1$, $A_2$ to $B_2$, etc.) corresponding to the marked profile lines in each of the stages in (a). Each graph shows misorientation, relative to the end point ($A_1$, $A_2$, etc.) as a function of distance. (c) $\langle 100 \rangle$ pole figures for the porphyroclasts for each time stage in (a). (d) Details of the process of subgrain rotation recrystallization, grain boundary sliding of recrystallized grains and overgrowth development (Stage 5 in (a)–(c)). The area shown corresponds to the higher-strain part of a porphyroclast.

spaces; the new garnet has an idiomorphic form; the source of the garnet is unclear; dissolution of garnet from boundaries in the shortening field, coupled with short range diffusion and re-precipitation (with a different composition) is suggested by the fact that many garnet grains have axial ratios >1, even when high-Ca overgrowths are ignored, although the continued existence of Ca-lows on these boundaries is difficult to explain; there may be net garnet growth related to ongoing metamorphic reactions.

(7) Small garnet grains continue to deform internally by dislocation creep mechanisms.

(8) Grain boundary sliding facilitates neighbour swapping and mechanical mixing so that garnet aggregates (morphology 3) evolve to stringers (morphology 4) and increasingly isolated small garnet grains (Fig. 12d).

(9) Rotation of individual garnet grains facilitates more complete overgrowths of Ca-rich garnet; the garnet is added piecemeal, as the grains rotate (Fig. 12d).

The data in this paper provide compelling evidence that garnet deforms plastically and can recrystallize to finer-grained garnet, which then deforms by a grain boundary sliding mechanism. Terry & Heidelbach (2004) suggested that a diffusion-accommodated grain boundary sliding mechanism would allow garnet to be significantly weaker than other phases. In their example, the mechanism is facilitated by the creation of fine-grained garnet through a metamorphic reaction. It is thus tempting to suggest that our data indicate that weakening can occur thorough the creation of finer grain sizes by plastic deformation and recrystallization. Fabrics are deflected around large garnet porphyroclasts (morphologies 1 and 2), whereas garnet aggregates and stringers (morphologies 3 and 4) play the same role in defining fabric as all other phases; thus, it seems reasonable, in the context of this study of the Glenelg sample, that garnet is weakened by the recrystallization process. However, it is unclear whether this process weakens the rock as a whole. Intra-grain plastic strain continues after recrystallization so that the mechanism of garnet deformation involves a balance between diffusion creep and dislocation creep (Casey & McGrew, 1999; De Bresser et al., 2001; Bestmann & Prior, 2003). The efficacy of the diffusion creep process is controlled by the grain size, which is, in turn, controlled by the subgrain rotation recrystallization mechanism.

## CONCLUSIONS

(1) Garnet can deform plastically to high strains at 700°C.
(2) Garnet can be recrystallized, by a subgrain rotation mechanism, to form finer-grained garnet.
(3) Recrystallization can facilitate a change in deformation mechanisms, so that diffusion-accommodated grain boundary sliding becomes important.
(4) Recrystallization may facilitate weakening in rocks where garnet is the dominant phase, such as postulated for the mantle Transition Zone.

## ACKNOWLEDGEMENTS

## REFERENCES

Adams, B. L., Wright, S. I. & Kunze, K. (1993). Orientation imaging: the emergence of a new microscopy. *Metallurgical Transactions A—Physical Metallurgy and Materials Science* **24**, 819–831.

Allen, F. M., Smith, B. K. & Buseck, P. R. (1987). Direct observations of dissociated dislocations in garnet. *Science* **238**, 1965–1967.

Ando, J., Fujino, K. & Takeshita, T. (1993). Dislocation microstructures in naturally deformed silicate garnets. *Physics of the Earth and Planetary Interiors* **80**, 105–116.

Ashby, M. F. & Verrall, R. A. (1973). Diffusion accommodated flow and superplasticity. *Acta Metallurgica* **21**, 149–163.

Ayres, M. & Vance, D. (1997). A comparative study of diffusion profiles in Himalayan and Dalradian garnets: constraints on diffusion data and the relative duration of the metamorphic events. *Contributions to Mineralogy and Petrology* **128**, 66–80.

Azor, A., Simancas, J. F., Exposito, I., Lodeiro, F. G. & Poyatos, D. J. M. (1997). Deformation of garnets in a low-grade shear zone. *Journal of Structural Geology* **19**, 1137–1148.

Bernardini, J. (1998). Segregation and grain boundary diffusion in metals and elemental semi-conductors. *Defect and Diffusion Forum* **156**, 49–50.

Bestmann, M. & Prior, D. J. (2003). Intragranular dynamic recrystallization in naturally deformed calcite marble: diffusion accommodated grain boundary sliding as a result of subgrain rotation recrystallization. *Journal of Structural Geology* **25**, 1597–1613.

Bocquet, L., Losert, W., Schalk, D., Lubensky, T. C. & Gollub, J. P. (2002). Granular shear flow dynamics and forces: experiment and continuum theory. *Physical Review E* **6501**, 011307.

Boullier, A. M. & Gueguen, Y. (1975). Origin of some mylonites by superplastic flow. *Contributions to Mineralogy and Petrology* **50**, 93–104.

Boyle, A. P., Prior, D. J., Banham, M. H. & Timms, N. E. (1998). Plastic deformation of metamorphic pyrite: new evidence from electron-backscatter diffraction and forescatter orientation–contrast imaging. *Mineralium Deposita* **34**, 71–81.

Brenker, F. E., Prior, D. J. & Muller, W. F. (2002). Cation ordering in omphacite and effect on deformation mechanism and lattice preferred orientation (LPO). *Journal of Structural Geology* **24**, 1991–2005.

Brewer, T. S., Storey, C. D., Parrish, R. R., Temperley, S. & Windley, B. F. (2003). Grenvillian age exhumation of eclogites in the Glenelg–Attadale Inlier, NW Scotland. *Journal of the Geological Society, London* **160**, 565–574.

Carstens, H. (1969). Dislocation structures in pyropes from Norwegian and Czech garnet peridotites. *Contributions to Mineralogy and Petrology* **24**, 348 *et seq.*

Carstens, H. (1971). Plastic stress relaxation around solid inclusions in pyrope. *Contributions to Mineralogy and Petrology* **32**, 289–294.

Casey, M. & McGrew, A. J. (1999). One-dimensional kinematic model of preferred orientation development. *Tectonophysics* **303**, 131–140.

Christensen, J. N., Selverstone, J., Rosenfeld, J. L. & DePaolo, D. J. (1994). Correlation by Rb–Sr geochronology of garnet growth histories from different structural levels within the Tauern Window, Eastern Alps. *Contributions to Mineralogy and Petrology* **118**, 1–12.

Daly, J. S., Cliff, R. A. & Yardley, B. W. D. (eds) (1989). *Evolution of Metamorphic Belts. Geological Society, London, Special Publications* **43**, 576 pp.

Dalziel, I. W. D. & Bailey, S. W. (1968). Deformed garnets in a mylonitic rock from the Grenville front and their tectonic significance. *American Journal of Science* **266**, 542–562.

De Bresser, J. H. P., Ter Heege, J. H. & Spiers, C. J. (2001). Grain size reduction by dynamic recrystallization: can it result in major rheological weakening? *International Journal of Earth Sciences* **90**, 28–45.

Deer, W. A., Howie, R. A. & Zussmann, J. (1992). *An Introduction to the Rock Forming Minerals*. Harlow: Longman, 696 pp.

DeWolf, C. P., Zeissler, C. J., Halliday, A. N., Mezger, K. & Essene, E. J. (1996). The role of inclusions in U–Pb and Sm–Nd garnet geochronology: stepwise dissolution experiments and trace uranium mapping by fission track analysis. *Geochimica et Cosmochimica Acta* **60**, 121–134.

Dingley, D. J. (1984). Diffraction from sub-micron areas using electron backscattering in a scanning electron-microscope. *Scanning Electron Microscopy*, Part 2, 569–575.

Dobbs, H. T., Peruzzo, L., Seno, F., Spiess, R. & Prior, D. J. (2003). Unraveling the Schneeberg garnet puzzle: a numerical model of multiple nucleation and coalescence. *Contributions to Mineralogy and Petrology* **146**, 1–9.

Doukhan, N., Sautter, V. & Doukhan, J. C. (1994). Ultradeep, ultramafic mantle xenoliths: transmission electron microscopy preliminary results. *Physics of the Earth and Planetary Interiors* **82**, 195–207.

Drury, M. & Humphreys, F. J. (1988). Microstructural shear criteria associated with grain boundary sliding during ductile deformation. *Journal of Structural Geology* **10**, 83–89.

Elliott, M. T., Cheadle, M. C. & Jerram, D. A. (1997). On the identification of textural equilibrium in rocks using dihedral angle measurements. *Geology* **25**, 355–358.

Fliervoet, T. F., White, S. H. & Drury, M. R. (1997). Evidence for dominant grain-boundary sliding deformation in greenschist- and amphibolite-grade polymineralic ultramylonites from the Redbank Deformed Zone, Central Australia. *Journal of Structural Geology* **19**, 1495–1520.

Fynn, G. W. & Powell, W. J. A. (1979). *The Cutting and Polishing of Electro-Optic Materials*. London: Adams Hilger, 216 pp.

Gifkins, R. C. (1973). Superplasticity, creep and grain-boundary sliding. *Scripta Metallurgica* **7**, 27–33.

Gifkins, R. C. (1976). Grain-boundary sliding and its accommodation during creep and superplasticity. *Metallurgical Transactions A—Physical Metallurgy and Materials Science* **7**, 1225–1232.

Gifkins, R. C. (1991). Ductility and strain-rate control mechanisms in superplasticity. *Scripta Metallurgica et Materialia* **25**, 1397–1400.

Gifkins, R. C. (1994). Grain-boundary participation in high-temperature deformation: an historical review. *Materials Characterization* **32**, 59–77.

Hirsch, D. M., Prior, D. J. & Carlson, W. D. (2003). An overgrowth model to explain multiple, dispersed high-Mn regions in the cores of garnet porphyroblasts. *American Mineralogist* **88**, 131–141.

Holness, M. B., Cheadle, M. J. & McKenzie, D. (2005). On the use of changes in dihedral angle to decode late-stage textural evolution in cumulates. *Journal of Petrology* **46**, 1565–1583.

Ji, S. C. & Martignole, J. (1994). Ductility of garnet as an indicator of extremely high-temperature deformation. *Journal of Structural Geology* **16**, 985–996.

Ji, S. C., Saruwatari, K., Mainprice, D., Wirth, R., Xu, Z. & Xia, B. (2003). Microstructures, petrofabrics and seismic properties of ultra high-pressure eclogites from Sulu region, China: implications for rheology of subducted continental crust and origin of mantle reflections. *Tectonophysics* **370**, 49–76.

Jiang, Z. T., Prior, D. J. & Wheeler, J. (2000). Albite crystallographic preferred orientation and grain misorientation distribution in a low-grade mylonite: implications for granular flow. *Journal of Structural Geology* **22**, 1663–1674.

Karato, S. & Wu, P. (1993). Rheology of the upper mantle: a synthesis. *Science* **260**, 771–778.

Karato, S., Wang, Z. C., Liu, B. & Fujino, K. (1995). Plastic-deformation of garnets: systematics and implications for the rheology of the mantle transition zone. *Earth and Planetary Science Letters* **130**, 13–30.

Kleinschrodt, R. & Duyster, J. P. (2002). HT-deformation of garnet: an EBSD study on granulites from Sri Lanka, India and the Ivrea Zone. *Journal of Structural Geology* **24**, 1829–1844.

Kleinschrodt, R. & McGrew, A. (2000). Garnet plasticity in the lower continental crust: implications for deformation mechanisms based on microstructures and SEM-electron channeling pattern analysis. *Journal of Structural Geology* **22**, 795–809.

Kohn, M. J., Catlos, E. J., Ryerson, F. J. & Harrison, T. M. (2001). Pressure–temperature–time path discontinuity in the Main Central thrust zone, central Nepal. *Geology* **29**, 571–574.

Lloyd, G. E. (1987). Atomic-number and crystallographic contrast images with the SEM: a review of backscattered electron techniques. *Mineralogical Magazine* **51**, 3–19.

Lloyd, G. E. & Freeman, B. (1991). SEM electron channeling analysis of dynamic recrystallization in a quartz grain. *Journal of Structural Geology* **13**, 945–953.

Lloyd, G. E., Schmidt, N. H., Mainprice, D. H., Olesen, N. H., Law, R. D. & Casey, M. (1991a). Textural determination via SEM electron channeling. *Textures and Microstructures* **14**, 213–218.

Lloyd, G. E., Schmidt, N. H., Mainprice, D. & Prior, D. J. (1991b). Crystallographic textures. *Mineralogical Magazine* **55**, 331–345.

Lloyd, G. E., Farmer, A. B. & Mainprice, D. (1997). Misorientation analysis and the formation and orientation of subgrain and grain boundaries. *Tectonophysics* **279**, 55–78.

Mainprice, D., Bascou, J., Cordier, P. & Tommasi, A. (2004). Crystal preferred orientations of garnet: comparison between numerical simulations and electron back-scattered diffraction (EBSD) measurements in naturally deformed eclogites. *Journal of Structural Geology* **26**, 2089–2102.

Marshall, D., Kirschner, D. & Bussy, F. (1997). A Variscan pressure–temperature–time path for the NE Mont Blanc massif. *Contributions to Mineralogy and Petrology* **126**, 416–428.

Matthews, M., Harte, B. & Prior, D. J. (1992). Mantle garnets: a cracking yarn. *Geochimica et Cosmochimica Acta* **56**, 2633–2642.

Mei, S., Bai, W., Hiraga, T. & Kohlstedt, D. L. (2002). Influence of melt on the creep behavior of olivine–basalt aggregates under hydrous conditions. *Earth and Planetary Science Letters* **201**, 491–507.

Okudaira, T. (1996). Temperature–time path for the low-pressure Ryoke metamorphism, Japan, based on chemical zoning in garnet. *Journal of Metamorphic Geology* **14**, 427–440.

Pattison, D. R. M. & Tracy, R. J. (1991). Phase-equilibria and thermobarometry of metapelites. *Reviews in Mineralogy* **26**, 105–206.

Poirier, J. P. & Guillope, M. (1979). Deformation induced recrystal-lization of minerals. *Bulletin de Mineralogie* **102**, 67–74.

Prior, D. J. (1993). Subcritical fracture and associated retrogression of garnet during mylonitic deformation. *Contributions to Mineralogy and Petrology* **113**, 545–556.

Prior, D. J. & Wheeler, J. (1999). Feldspar fabrics in a greenschist facies albite-rich mylonite from electron backscatter diffraction. *Tectonophysics* **303**, 29–49.

Prior, D. J., Trimby, P. W., Weber, U. D. & Dingley, D. J. (1996). Orientation contrast imaging of microstructures in rocks using forescatter detectors in the scanning electron microscope. *Mineralogical Magazine* **60**, 859–869.

Prior, D. J., Boyle, A. P., Brenker, F., Cheadle, M. C., Day, A., Lopez, G., *et al.* (1999). The application of electron backscatter diffraction and orientation contrast imaging in the SEM to textural problems in rocks. *American Mineralogist* **84**, 1741–1759.

Prior, D. J., Wheeler, J., Brenker, F. E., Harte, B. & Matthews, M. (2000). Crystal plasticity of natural garnet: new microstructural evidence. *Geology* **28**, 1003–1006.

Prior, D. J., Wheeler, J., Peruzzo, L., Spiess, R. & Storey, C. (2002). Some garnet micro structures: an illustration of the potential of orientation maps and misorientation analysis in microstructural studies. *Journal of Structural Geology* **24**, 999–1011.

Rawson, J. R., Carswell, D. A. & Smallwood, D. (2001). Garnet-bearing olivine–websterite within the Eastern Glenelg Lewisian of the Glenelg Inlier, NW Highlands. *Scottish Journal of Geology* **37**, 27–34.

Read, H. H. (1970). *Rutley's Elements of Mineralogy*. London: Thomas Murbo, 560 pp.

Ross, I. M., Rainforth, W. M., McComb, D. W., Scott, A. J. & Brydson, R. (2001). Grain boundary segregation in $Al_2O_3$ doped 3Y-TZP ceramics, electron microscopy and analysis 2001. *Institute of Physics Conference Series*, 299–302.

Ross, J. V. (1973). Mylonitic rocks and flattened garnets in the southern Okanagan of British Columbia. *Canadian Journal of Earth Sciences* **10**, 1–17.

Sammis, C. G. (2001). Materials science issues in the Earth and Planetary sciences. *Progress in Materials Science* **46**, 231–247.

Sanders, I. S. (1988). Plagioclase breakdown and regeneration reactions in Grenville kyanite eclogite at Glenelg, NW Scotland. *Contributions to Mineralogy and Petrology* **98**, 33–39.

Sanders, I. S. (1989). Phase relations and *P–T* conditions for eclogite-facies rocks at Glenelg, north-west Scotland. In: Daly, J. S., Cliff, R. A. & Yardley, B. W. D. (eds) *Evolution of Metamorphic Belts. Geological Society, London, Special Publications* **43**, 513–517.

Sanders, I. S., Van Calsteren, P. W. C. & Hawkesworth, C. J. (1984). A Grenville Sm–Nd age for the Glenelg Eclogite in Northwest Scotland. *Nature* **312**, 439–440.

Scherer, E. E., Cameron, K. L. & Blichert-Toft, J. (2000). Lu–Hf garnet geochronology: closure temperature relative to the Sm–Nd system and the effects of trace mineral inclusions. *Geochimica et Cosmochimica Acta* **64**, 3413–3432.

Shodja, H. M. & Nezami, E. G. (2003). A micromechanical study of rolling and sliding contacts in assemblies of oval granules. *International Journal for Numerical and Analytical Methods in Geomechanics* **27**, 403–424.

Smith, B. K. (1982). Plastic deformation of garnets: mechanical behaviour and associated microstructures. Ph.D. thesis, University of California, Berkeley.

Spear, F. S. (1992). Thermobarometry and *P–T* paths from granulite facies rocks: an introduction. *Precambrian Research* **55**, 201–207.

Spear, F. S. & Selverstone, J. (1983). Quantitative *P–T* paths from zoned minerals: theory and tectonic applications. *Contributions to Mineralogy and Petrology* **83**, 348–357.

Spiess, R., Peruzzo, L., Prior, D. J. & Wheeler, J. (2001). Development of garnet porphyroblasts by multiple nucleation, coalescence and boundary misorientation-driven rotations. *Journal of Metamorphic Geology* **19**, 269–290.

Storey, C. D. (2002). Tectono-metamorphic evolution of the Glenelg–Attadale Inlier, northwest Scotland. Ph.D. thesis, University of Leicester.

Storey, C. D., Brewer, T. S. & Temperley, S. (2005). *P–T* conditions of Grenville-age eclogite facies metamorphism and amphibolite facies retrogression of the Glenelg–Attadale Inlier, NW Scotland. *Geological Magazine*, in press.

Sutton, A. P. & Balluffi, R. W. (1995). *Interfaces in Crystalline Materials*. Oxford: Oxford Science Publications, 819 pp.

Terry, M. P. & Heidelbach, F. (2004). Superplasticity in garnet from eclogite facies shear zones in the Haram Gebbro, Haramsøya, Norway. *Geology* **32**, 281–284.

Trepmann, C. A. & Stöckhert, B. (2002). Cataclastic deformation of garnet: a record of synseismic loading and postseismic creep. *Journal of Structural Geology* **24**, 1845–1856.

Trimby, P. W., Prior, D. J. & Wheeler, J. (1998). Grain boundary hierarchy development in a quartz mylonite. *Journal of Structural Geology* **20**, 917–935.

Urai, J. L. & Jessell, M. (2001). Recrystallization and grain growth in minerals: recent developments. In: Gottstein, G. & Molodov, D. (eds) *Proceedings of the First Joint International Conference on Recrystallization and Grain Growth*. Berlin: Springer Verlag, pp. 87–95.

Urai, J. L., Means, W. D. & Lister, G. S. (1986). Dynamic recrystallization of minerals. In: Hobbs, B. E. & Heard, H. C. (eds) *Mineral and Rock Deformation (Laboratory Studies)*. *Geophysical Monograph, American Geophysical Union* **36**, 161–200.

Vance, D. (1995). Rate and time controls on metamorphic processes. *Geological Journal* **30**, 241–259.

Vance, D. & Holland, T. (1993). A detailed isotopic and petrological study of a single garnet from the Gassetts Schist, Vermont. *Contributions to Mineralogy and Petrology* **114**, 101–118.

Vance, D. & Mahar, E. (1998). Pressure–temperature paths from *P–T* pseudosections and zoned garnets: potential, limitations and examples from the Zanskar Himalaya, NW India. *Contributions to Mineralogy and Petrology* **132**, 225–245.

Vance, D. & O'Nions, R. K. (1988). Chronometry of single zoned garnets: constraints on growth-kinetics and metamorphic histories. *Chemical Geology* **70**, 82.

Vance, D. & O'Nions, R. K. (1990). Isotopic chronometry of zoned garnets: growth-kinetics and metamorphic histories. *Earth and Planetary Science Letters* **97**, 227–240.

Vance, D., Meier, M. & Oberli, F. (1998). The influence of high U–Th inclusions on the U–Th–Pb systematics of almandine–pyrope garnet: results of a combined bulk dissolution, stepwise-leaching, and SEM study. *Geochimica et Cosmochimica Acta* **62**, 3527–3540.

Vauchez, A. & Mainprice, D. (1996). Dynamics of the subcontinental mantle: from seismic anisotropy to mountain building—preface. *Physics of the Earth and Planetary Interiors* **95**, 123–125.

Venables, J. A. & Harland, C. J. (1973). Electron backscattering patterns: a new technique for obtaining crystallographic information in the SEM. *Philosophical Magazine* **27**, 1193–1200.

Voegele, V., Ando, J. I., Cordier, P. & Liebermann, R. C. (1998*a*). Plastic deformation of silicate garnets I: high-pressure experiments. *Physics of the Earth and Planetary Interiors* **108**, 305–318.

Voegele, V., Cordier, P., Sautter, V., Sharp, T. G., Lardeaux, J. M. & Marques, F. O. (1998*b*). Plastic deformation of silicate garnets II: deformation microstructures in natural samples. *Physics of the Earth and Planetary Interiors* **108**, 319–338.

Voegele, V., Liu, B., Cordier, P., Wang, Z., Takei, H., Pan, P. & Karato, S. (1999). High temperature creep in a 2–3–4 garnet: $Ca_3Ga_2Ge_3O_{12}$. *Journal of Materials Science* **34**, 4783–4791.

Voegele, V., Cordier, P., Langenhorst, F. & Heinemann, S. (2000). Dislocations in meteoritic and synthetic majorite garnets. *European Journal of Mineralogy* **12**, 695–702.

Wheeler, J., Prior, D. J., Jiang, Z., Spiess, R. & Trimby, P. W. (2001). The petrological significance of misorientations between grains. *Contributions to Mineralogy and Petrology* **141**, 109–124.

White, S. (1977). Geological significance of recovery and recrystallization processes in quartz. *Tectonophysics* **39**, 143–170.

Whitney, D. L. (1996). Garnets as open systems during regional metamorphism. *Geology* **24**, 147–150.

Wynblatt, P., Rohrer, G. S. & Papillon, F. (2003). Grain boundary segregation in oxide ceramics. *Journal of the European Ceramic Society* **23**, 2841–2848.

Yardley, B. W. D. (1977). Empirical study of diffusion in garnet. *American Mineralogist* **62**, 793–800.